Atmospheric
Chemistry
and Physics
Open Access
Discussions

Inferring regional sources and sinks of atmospheric CO2 from GOSAT XCO2 data

F. Deng[1], D. B. A. Jones[1,2], D. K. Henze[3], N. Bousserez[3], K. W. Bowman[4,2], J. B. Fisher[4], R. Nassar[5], C. O'Dell[6], D. Wunch[7], P. O. Wennberg[7], E. A. Kort[8], S. C. Wofsy[9], T. Blumenstock[10], N. M. Deutscher[11,12], D. Griffith[12], F. Hase[10], P. Heikkinen[13], V. Sherlock[14], K. Strong[1], R. Sussmann[15], and T. Warneke[11]

[1]Department of Physics, University of Toronto, Toronto, ON, Canada
[2]Joint Institute for Regional Earth System Science and Engineering, University of California, Los Angeles, CA, USA
[3]Department of Mechanical Engineering, University of Colorado, Boulder, CO, USA
[4]Jet Propulsion Laboratory, California Institute of Technology, Pasadena, CA, USA
[5]Climate Research Division, Environment Canada, Toronto, ON, Canada
[6]Colorado State University, USA
[7]California Institute of Technology, Pasadena, CA, USA
[8]Department of Atmospheric, Oceanic and Space Sciences, University of Michigan, Ann Arbor, MI, USA
[9]Harvard University, Cambridge, MA, USA
[10]Karlsruhe Institute of Technology (KIT), Institute for Meteorology and Climate Research (IMK-ASF), Karlsruhe, Germany

Discussion Paper | Discussion Paper | Discussion Paper | Discussion Paper |

ACPD

13, 26327–26388, 2013

Inferring CO2 fluxes from GOSAT XCO2

F. Deng et al.

Title Page

Abstract | Introduction

Conclusions | References

Tables | Figures

◀ | ▶

◀ | ▶

Back | Close

Full Screen / Esc

Printer-friendly Version

Interactive Discussion

[11]Institute of Environmental Physics, University of Bremen, Bremen, Germany
[12]School of Chemistry, University of Wollongong, NSW, Australia
[13]FMI-Arctic Research Center, Sodankylä, Finland
[14]National Institute of Water and Atmospheric Research, Wellington, New Zealand
[15]IMK-IFU, Garmisch-Partenkirchen, Germany

Correspondence to: F. Deng (dengf@atmosp.physics.utoronto.ca)

Inferring CO$_2$ fluxes from GOSAT XCO$_2$

F. Deng et al.

Printer-friendly Version

Interactive Discussion

Abstract

We have examined the utility of retrieved column-averaged, dry-air mole fractions of CO$_2$ (XCO$_2$) from the Greenhouse Gases Observing Satellite (GOSAT) for quantifying monthly, regional flux estimates of CO$_2$, using the GEOS-Chem four-dimensional variational (4D-Var) data assimilation system. We focused on assessing the potential impact of biases in the GOSAT CO$_2$ data on the regional flux estimates. Using different screening and bias correction approaches, we selected three different subsets of the GOSAT XCO$_2$ data for the 4D-Var inversion analyses, and found that the inferred global fluxes were consistent across the three XCO$_2$ inversions. However, the GOSAT observational coverage was a challenge for the regional flux estimates. In the northern extratropics, the inversions were more sensitive to North American fluxes than to European and Asian fluxes due to the lack of observations over Eurasia in winter and over eastern and southern Asia in summer. The regional flux estimates were also sensitive to the treatment of the residual bias in the GOSAT XCO$_2$ data. The largest differences obtained were for Temperate North America and Temperate South America, for which the largest spread between the inversions was 1.02 Pg C and 0.96 Pg C, respectively. In the case of Temperate North America, one inversion suggested a strong source, whereas the second and third XCO$_2$ inversions produced a weak and strong sink, respectively. Despite the discrepancies in the regional flux estimates between the three XCO$_2$ inversions, the a posteriori CO$_2$ distributions were in good agreement (with a mean difference between the three inversions of typically less than 0.5 ppm) with independent data from the Total Carbon Column Observing Network (TCCON), the surface flask network, and from the HIAPER Pole-to-Pole Observations (HIPPO) aircraft campaign. The discrepancy in the regional flux estimates from the different inversions, despite the agreement of the global flux estimates, suggests the need for additional work to determine the minimum spatial scales at which we can reliably quantify the fluxes using GOSAT XCO$_2$. The fact that the a posteriori CO$_2$ from the different inversions were in good agreement with the independent data although the regional flux estimates dif-

fered significantly, suggests that innovative ways of exploiting existing datasets, and possibly additional observations, are needed to better evaluate the inferred regional flux estimates.

1   Introduction

5   The steady increase of atmospheric CO_2 during the past 200 yr is an important contributor to climate change. However, in the past half century only about 45 % of the anthropogenic emissions have remained in the atmosphere (Jones et al., 2005; Canadell et al., 2007), the remainder absorbed by the oceans and/or fixed by the terrestrial biosphere. Information on the spatial and temporal distribution of the carbon flux is critical
10   to understanding the dominant processes governing the variability of the global carbon cycle, and hence improves our ability to predict future global climate change.

The flask atmospheric CO_2 concentration observations have been one of the most important datasets in quantifying and understanding the global carbon cycle. These data have been intensively used in estimating global and regional carbon sinks and
15   sources via various kinds of atmospheric inversions (e.g. Enting et al., 1995; Fan et al., 1998; Rayner et al., 1999; Gurney et al., 2002; Peylin et al., 2002; Rödenbeck et al., 2003; Law et al., 2003; Patra et al., 2005; Michalak et al., 2005; Baker et al., 2006b; Peters et al., 2007; Deng and Chen, 2011; Bruhwiler et al., 2011). Though there is general agreement in the estimates of hemispheric-scale fluxes, large uncertainties
20   still remain in the estimates of the fluxes on smaller, regional scales, due partly to the limited spatial scale of the observations, errors in the atmospheric models (e.g. Stephens et al., 2007), and to the different configurations of the atmospheric inversions.

Space-based observations of CO_2 provide greater observational coverage than the surface observational network, and several studies (e.g., Park and Prather, 2001;
25   Rayner and O'Brien, 2001; Houweling et al., 2004; Baker et al., 2006a; Chevallier et al., 2007) have suggested that these data will offer greater constraints on estimates of regional sources and sinks of CO_2. Nassar et al. (2011) showed that observations from

the Tropospheric Emission Spectrometer (TES) provide useful additional information on CO$_2$ sources and sinks, particularly in the tropics, where the density of the surface network is sparse. The additional reduction in uncertainty on estimates of the fluxes obtained by Nassar et al. (2011) was more limited in the extratropics, which could be

5   due to the fact that they used only ocean data between 40° S–40° N, so the observational coverage was limited. Chevallier et al. (2009) conducted an inversion analysis of CO$_2$ data from the Atmospheric Infrared Sounder (AIRS) and found that it did not improve estimates of the CO$_2$ fluxes, beyond what they obtained from assimilating data from the surface network. A major challenge with use of the data from space-based

10 thermal infrared instruments such as TES and AIRS is that these instruments were not designed for observing atmospheric CO$_2$ near the surface, and hence the information content of the CO$_2$ abundances retrieved from their measurements is limited. Although improved retrievals algorithms may eventually provide better results for the middle and upper troposphere, sensitivity to the lower troposphere will remain elusive.

15 The Greenhouse Gases Observing Satellite (GOSAT) (Kuze et al., 2009), launched on 23 January 2009, was designed to monitor total atmospheric columns carbon dioxide (CO$_2$) and methane (CH$_4$) globally from space. Recent inversion analyses (Takagi et al., 2011; Maksyutov et al., 2012; Basu et al., 2013) have shown that the total column CO$_2$ abundances inferred from GOSAT measurements can provide constraints on

20 CO$_2$ flux estimates that are complementary to those obtained from surface observations. We present here an investigation of the impact of biases in the GOSAT CO$_2$ data on regional flux estimates of CO$_2$. We use retrievals of the column-averaged dry-air mole fractions of CO$_2$ (XCO$_2$) produced by the NASA Atmospheric CO$_2$ Observations from Space (ACOS) project for July 2009 – December 2010, together with the GEOS-

25 Chem model, to quantify monthly estimates of regional fluxes of CO$_2$ for 2010. We also employ observations from the surface flask network and compare the fluxes inferred from the flask data with those obtained from the GOSAT XCO$_2$ data product. The results of the inversion analyses are evaluated using independent data from the Total Carbon Column Observing Network (TCCON) and the HIAPER Pole-to-Pole Observa-

tions (HIPPO) project. We also compare our inferred flux estimates in the extratropics with a global flux dataset derived from eddy covariance measurements (Jung et al., 2011).

The rest of this article is organized as follows. Section 2 summarizes the retrieval algorithm and datasets used to constrain the model, and to evaluate our modeling results. Section 3 presents the estimated carbon fluxes and the evaluation of performance of the inverse modeling. Regional flux estimates and their sensitivities are discussed in Sect. 4. Conclusions are presented in Sect. 5.

2 Methods and data

2.1 Observations and their uncertainties

2.1.1 Satellite observations

The GOSAT spacecraft (Kuze et al., 2009), launched January 2009, is dedicated to measuring carbon dioxide (CO_2) and methane (CH_4), using the Thermal and Near Infrared Sensor for Carbon Observation Fourier-Transform Spectrometer (TANSO-FTS). The TANSO-FTS detects gas absorption in the short wave infrared (SWIR) and thermal infrared (TIR) region of the spectrum. The SWIR consists mainly of reflected solar radiation and therefore, provides sensitivity to variations in the abundance of CO_2 throughout the troposphere and down into the boundary layer. GOSAT is in a sun-synchronous polar orbit at an altitude of 666 km, with a repeat cycle of 3 days.

We use here the NASA Atmospheric CO_2 Observations from Space (ACOS) GOSAT XCO$_2$ data product, spanning July 2009 to December 2010. The ACOS retrievals employ an optimal estimation approach to infer atmospheric profile abundances of CO_2, from which the total column dry-air mole fraction (XCO$_2$) is calculated. The details of the retrieval are described in O'Dell et al. (2012). The retrieved CO_2 profile is given by

$$\hat{\boldsymbol{y}} = \boldsymbol{y}_a + \mathbf{A}(\boldsymbol{y} - \boldsymbol{y}_a), \tag{1}$$

where $\boldsymbol{y}$ is the true CO_2 profile (on a 20-level vertical grid), $\boldsymbol{y}_a$ is the a priori profile used in the retrieval, and $\mathbf{A}$ is the averaging kernel matrix, which gives the sensitivity of the retrieved CO_2 to the true CO_2. From Eq. (1) the XCO_2 can be calculated as

$$XCO_2 = \frac{\int_0^{P_{\text{surf}}}[\boldsymbol{y}_a + \mathbf{A}(\boldsymbol{y} - \boldsymbol{y}_a)](1-q)\mathrm{d}p}{\int_0^{P_{\text{surf}}}(1-q)\mathrm{d}p}, \tag{2}$$

where q is the water vapour mixing ratio and p is the air pressure. Equation (2) can be written as (Connor et al., 2008)

$$XCO_2 = XCO_2^a + \sum_j \mathbf{h}_j \mathbf{a}_{CO_2,j}(\boldsymbol{y} - \boldsymbol{y}_a)_j, \tag{3}$$

where $\mathbf{h}_j$ is the contribution of the normalized pressure weighting function for retrieval layer j, $\mathbf{a}_{CO_2,j}$ is the normalized column averaging kernel (defined as $\mathbf{a}_{CO_2,j} = (\mathbf{h}^T\mathbf{A})_j/\mathbf{h}_j$), and XCO_2^a is the a priori CO_2 column assumed by the retrieval ($XCO_2^a = \mathbf{h}^T\boldsymbol{y}_a$). The pressure weighting function corrects for the presence of water vapour, as described in the denominator of Eq. (2), using the water vapour inferred by the retrieval algorithm.

To assess the impact of residual bias in the XCO_2 retrievals on regional flux estimates, we use versions b2.9 and b2.10 of the ACOS product. ACOS b2.10 is similar to b2.9 version described in (O'Dell et al., 2012), with a couple important changes: the aerosol scheme was modified to allow more flexibility to deviate from the aerosol prior, the gas absorption models were updated (Thompson et al., 2012), and the prior CO_2 profile was changed to agree with that of TCCON (Wunch et al., 2010). In addition, the filtering and bias correction schemes were refined and updated for version b2.10. We use only the "High gain" (H-gain) data, which excludes data over bright surfaces, such as deserts, and we neglect the glint observations, that provide coverage over oceans since their biases are not as well-quantified. For the b2.9 data, we screened

|◄ | ►|

◄ | ►

Back | Close

Full Screen / Esc

and corrected the bias in the data in the following two ways: (a) we screened out data with retrieved surface pressure (P_{surf}) that differs from the European Centre for Medium Range Weather Forecasting (ECMWF) surface pressure by more than 5 hPa (Wunch et al., 2011); and (b) we corrected the data using the four-parameter bias-correction proposed by Wunch et al. (2011), but with the four coefficients calculated based on the data used in this study. Other than the surface pressure difference mentioned above, we used the same filter criteria according to Wunch et al. (2011) in (a) and (b). The filtered b2.9, filtered and bias corrected b2.9 and the b2.10 data used here will be referred to as XCO2_A, XCO2_B, and XCO2_C, respectively. Figure 1 shows the zonal mean XCO_2 of four XCO_2 datasets based on different filtering and bias correction approaches. Selecting data with surface pressure errors that are less than 5 hPa reduced the XCO_2 values in the tropics and subtropics in between spring and fall (April–November in the Northern Hemisphere and November–May in the Southern Hemisphere). Application of the Wunch et al. (2011) bias correction (in XCO2_B) further reduced the XCO_2 values in these regions. In contrast, the bias correction in XCO2_B resulted in increases in extratropical XCO_2 in the Northern Hemisphere in winter. XCO_2 values in XCO2_C in general are higher than that in XCO2_A and XCO2_B.

2.1.2 Flask observations

We use here CO_2 mixing ratios measured by a non-dispersive infrared absorption technique in air samples collected in glass flasks at NOAA ESRL Carbon Cycle Cooperative Global Air Sampling Network sites (Conway et al., 2011) and Environment Canada (EC) sampling sites. The 72 NOAA sites and six EC sites are shown in Fig. 2. The flask measurements are directly traceable to the World Meteorological Organization (WMO) CO_2 mole fraction scale (WMO X2007) (Zhao and Tans, 2006). Measurement accuracy determined from repeated analyses of CO_2 in standard gas cylinders using an absolute manometric technique is ~ 0.2 ppm. Measurement precision determined from repeated NDIR analysis of the same air is ~ 0.1 ppm. Average agreement between pairs of flasks sampled in series throughout the network is currently ~ 0.1 ppm.

Therefore, the accuracy and precision of flask measurements are undoubtedly high. When the observations are compared with the modeled observations, the model-data mismatches for the observations are larger, since representativeness errors must be accounted for.

The uncertainties assigned to these data for inverse modeling are calculated using the statistics of the differences between the observations and the model simulations of the observations using the a priori emissions (Palmer et al., 2003; Heald et al., 2005). We calculated these uncertainties following the procedures detailed by Nassar et al. (2011), and these values are further scaled down to 68 % as the uncertainties used in our inverse modeling.

2.1.3 TCCON observations

We use XCO_2 data from TCCON observatories to evaluate our inferred CO_2 surface fluxes by examining whether the a posteriori CO_2 distribution is in better agreement with the TCCON data. The TCCON sites use ground-based Fourier transform spectrometers to measure high resolution spectra ($0.02\,cm^{-1}$) in the near infrared (3800–$15\,500\,cm^{-1}$), from which XCO_2 is retrieved. A profile scaling retrieval approach is used to calculate the column CO_2 abundance. The column-averaged dry air mole fraction is then is computed as (Wunch et al., 2011)

$$XCO_2 = 0.2095 \cdot \frac{CO_2^{col}}{O_2^{col}}, \tag{4}$$

where O_2^{col} is the simultaneously retrieved atmospheric oxygen column density, and 0.2095, is the nominal, globally-averaged (column-averaged) mole fraction of O_2. TCCON XCO_2 have been rigorously calibrated against the integrated profiles of CO_2 measured by WMO-standard instrumentation aboard aircraft (Wunch et al., 2010; Washenfelder et al., 2006; Deutscher et al., 2010; Messerschmidt et al., 2011). The TCCON

precision and accuracy in the calibrated $X\text{CO}_2$ data are both 0.8 ppm (2σ) (Wunch et al., 2010).

2.1.4 HIPPO aircraft measurements

The HIAPER Pole-to-Pole Observations (HIPPO) project is a sequence of five global aircraft measurement campaigns that sample the atmosphere from near the North Pole to the coastal waters of Antarctica, from the surface to 14 km (Wofsy et al., 2011). The NCAR/NSF High-performance Instrumented Airborne Platform for Environmental Research (HIAPER), a modified Gulfstream V (GV) jet hosted the HIPPO campaigns. Major GHGs (CO_2, CH_4, N_2O) and other important trace species were measured at high frequency, with two (or more) independent measurements for each to provide redundancy, check calibration and assess sensor drift. We use the CO_2 field based on one-second data averaged to 10 s, from two (harmonized) sensors: CO_2-QCLS and CO_2-OMS. UTC (time), GGLAT (latitude from GPS), GGLON (longitude from GPS), and PSXC (static pressure) are the fields that we used to match observation with modeled CO_2 mixing ratio. In Sect. 3.2.2, we compare our results with data observed from campaign 3 (HIPPO-3) in March and April 2010, and the route of the campaign is shown in Fig. 2.

2.1.5 Eddy covariance-based observations

We compare to land-atmosphere CO_2 fluxes from a so-called "upscaled" eddy covariance global product (MPI-BGC: Jung et al., 2009; Jung et al., 2011). This product derives a globally-gridded, time varying dataset from in situ measurements of net ecosystem exchange (NEE) at hundreds of flux tower sites worldwide. The towers' instruments (sonic anemometer, infrared gas analyzer) measure fluxes on the order of 1 km, in addition to ancillary measurements (e.g., meteorology) and other fluxes (Baldocchi et al., 2001; Baldocchi, 2008). The MPI-BGC product is derived from a suite of statistical model decision trees that link predictive variables (primarily air temperature, precipita-

tion, and fraction of absorbed photosynthetically active radiation) available at the global scale to the NEE fluxes, and also derives Gross Primary Production (GPP) and Total Ecosystem Respiration (TER) products. The MPI-BGC product can be used only for specific analyses as the world is treated somewhat unrepresentatively like a flux site,

5 e.g., undistorted, growing, flat, biased towards temperate regions; the mean annual flux, for instance, is not appropriate to compare to. Nonetheless, the MPI-BGC product is valuable for assessing relative spatial distributions, seasonal variability, and timing of min/max uptake, amplitude of the max-min uptake, interannual variability, and hotspots.

2.2 Forward modeling

10 The GEOS-Chem model (http://geos-chem.org) is used to simulate global atmospheric CO$_2$. The model is a global 3-D chemical transport model driven by assimilated meteorology from the Goddard Earth Observing System (GEOS-5) of the NASA Global Modeling and Assimilation Office (GMAO). Nassar et al. (2010) described the recent update of the atmospheric CO$_2$ simulation in GEOS-Chem. In this study, we employ

15 the model at a horizontal resolution of 4° × 5°, with 47 vertical layers. Our model simulations include CO$_2$ fluxes from fossil fuel combustion and cement production, from ocean surface exchange, from terrestrial biosphere assimilation and respiration, and from biomass burning. Specifically, these include (i) monthly national fossil fuel and cement manufacture CO$_2$ emission from the Carbon Dioxide Information Analysis Center

20 (CDIAC) (Andres et al., 2011); (ii) monthly shipping emissions of CO$_2$ from the International Comprehensive Ocean–Atmosphere Data Set (ICOADS) (Corbett and Koehler, 2003; Corbett, 2004; Endresen et al., 2004, 2007); (iii) 3-D aviation CO$_2$ emissions (Kim et al., 2007; Wilkerson et al., 2010; Friedl, 1997); (iv) monthly mean biomass burning CO$_2$ emissions from the Global Emissions Fire Database version 3 (GFEDv3)

25 (van der Werf et al., 2010); (v) biofuel (heating/cooking) CO$_2$ emission estimated by Yevich and Logan (2003); (vi) the flux of CO$_2$ across the air–water interface based on the climatology of monthly ocean-atmosphere CO$_2$ flux by Takahashi et al. (2009); and (vii) 3 hourly terrestrial ecosystem exchange produced by the Boreal Ecosystem

Productivity Simulator (BEPS) (Chen et al., 1999), which was driven by NCEP reanalysis data (Kalnay et al., 1996) and remotely sensed leaf area index (LAI) (Deng et al., 2006). The annual terrestrial ecosystem exchange imposed in each grid box is neutral (Deng and Chen, 2011). The emission inventories for 2010 used in our GEOS-Chem simulation are summarized in Table 1.

2.3 Inverse problem and optimizing method

In the inversion analysis, the surface CO_2 sources and sinks (x) are related to the atmospheric observations (y) by the following relationship

$$y = H(x) + \varepsilon, \tag{5}$$

where H is the forward atmospheric model (such as GEOS-Chem) and ε is the observation error, or model-data mismatch, which reflects the difference between the observations and the modelled results, including errors associated with observations (instrument errors) and model errors. Considering an a priori estimate of the CO_2 flux x_a, we can construct a cost function

$$J(x) = \frac{1}{2}(H(x) - y)^T \mathbf{S}_o^{-1}(H(x) - y) + \frac{1}{2}(x - x_a)^T \mathbf{S}_a^{-1}(x - x_a), \tag{6}$$

where y is a the vector of observations and $\mathbf{S}_o$ and $\mathbf{S}_a$ are the observational and a priori error covariance matrixes, respectively. Minimization of the cost function, subject to the a priori constraint, provides an optimal estimate of the fluxes, based on the available observations.

In the version of GEOS-Chem employed here, we use a 4-dimensional variational (4D-var) data assimilation system in which we optimize a set of scaling factors to adjust the fluxes in each model grid box to better reproduce the observations over a given time period. The 4D-var cost function that we minimize is given by

$$J(c) = \frac{1}{2}\sum_{i=1}^{N}(f_i(c) - y_i)^T \mathbf{S}_{0,i}^{-1}(f_i(c) - y_i) + \frac{1}{2}(c - c_a)^T (\mathbf{S}_a^c)^{-1}(c - c_a), \tag{7}$$

where N is the number of observations, $\boldsymbol{y}_i$, distributed in time over the assimilation window, $\boldsymbol{c}$ is the state vector of scaling factors, and $\boldsymbol{c}_a$ is the vector of a priori scaling factors, which we typically assume are unity. The a posteriori flux estimate for the jth grid cell is thus given by $\boldsymbol{x}_j = \boldsymbol{c}_j \boldsymbol{x}_{a,j}$. Here the forward model f includes the observation operator that maps the modeled CO_2 profile to the GOSAT XCO_2 observation space

$$XCO_2^m = f(\boldsymbol{x}) = XCO_2{}^a + \sum_j \boldsymbol{h}_j \boldsymbol{a}_{CO_2,j}(H(\boldsymbol{x}) - \boldsymbol{y}_a)_j, \tag{8}$$

which is analogous to Eq. (3), with the modeled CO_2 profile $H(\boldsymbol{x})$ interpolated onto the GOSAT retrieval levels. Here XCO_2^m is the modelled XCO_2, $\boldsymbol{a}_{CO_2}$ is the GOSAT column averaging kernel, and $\boldsymbol{h}$ is the pressure weighting function provided with each GOSAT XCO_2 retrieval.

The cost function is minimized iteratively using the L-BFGS algorithm (Liu and Nocedal, 1989) together with the adjoint of GEOS-Chem (Henze et al., 2007). The adjoint provides an efficient way to compute the sensitivity of the model output to inputs and model parameters, and was originally developed and used to optimize aerosol and CO sources (Henze et al., 2007, 2009; Kopacz et al., 2009, 2011; Jiang et al., 2011). In this work, we apply the adjoint to optimize global surface CO_2 sinks and sources.

In constructing the observational error covariance $\boldsymbol{S}_0$, we used the XCO_2 error estimates provided with the ACOS-GOSAT dataset. However, these errors were uniformly inflated to ensure that the a posteriori reduced $\chi^2 = 1$ constraint (Tarantola, 2004) was approximately satisfied. This scaling is justified since the observation errors (or the model-data mismatches) incorporate errors associated with observations and the model, which is difficult to characterize. For inversion of the XCO2_A, XCO2_B, and XCO2_C datasets, we inflated the reported ACOS XCO_2 errors by 1.7, 1.57 and 1.175, respectively.

The state vector in the inversion consists of the sum of CO_2 fluxes from fossil fuel combustion and cement manufacture, biofuel burning, biomass burning, exchange with the terrestrial biosphere, and exchange with the ocean. As with the observational error

covariance matrix, the a priori uncertainty estimates for these components of $\mathbf{S}_a$ were adjusted to ensure that the a posteriori reduced $\chi^2 = 1$ constraint was satisfied and to balance the observational term in the cost function. According to Marland et al. (2008), the uncertainty for estimates of global fossil fuel emissions is about 6 %. However, in constructing $\mathbf{S}_a$, we assigned 16 % for the uncertainty of the fossil fuel emissions in each month and each model grid box. For biomass burning, we started with an assumed uncertainty of 20 % that was then inflated to 38 % for emissions in each month and in each model grid box. The annual GPP estimate for 2010 is −119.5 Pg C and we assigned an uncertainty of 22 % of the GPP estimates in each 3 h time step and in each model grid. The TER, which is the sum of autotrophic and heterotrophic respiration, was specified to be 119.5 Pg C in 2010 since we assumed an annual balanced biosphere. We also assigned 22 % of the prior estimates in each 3 h time step and in each model grid as the prior TER uncertainty. For the ocean flux we assumed an a priori uncertainty of 44 %.

2.4   A posteriori uncertainty estimation

The optimization algorithm requires calculating the gradient of the cost function

$$\nabla J(\boldsymbol{c}) = \sum_{i=1}^{N} \mathbf{K}_i^T \mathbf{S}_{0,i}^{-1} (\mathbf{K}_i \boldsymbol{c}_i - \boldsymbol{y}_i) + (\mathbf{S}_a^c)^{-1} (\boldsymbol{c} - \boldsymbol{c}_a), \tag{9}$$

where $\mathbf{K}_i$ is the Jacobian associated with the linearization of the observation operator (forward atmospheric model) f_i. The second derivative of the cost function is the Hessian,

$$\nabla^2 J(\boldsymbol{c}) = \sum_{i=1}^{N} \mathbf{K}_i^T \mathbf{S}_{0,i}^{-1} \mathbf{K}_i + (\mathbf{S}_a^c)^{-1}, \tag{10}$$

and for a linear system, such as CO_2 transport, the a posteriori error covariance matrix is given by the inverse of the Hessian,

$$\hat{\mathbf{S}} = \left(\sum_{i=1}^{N} \mathbf{K}_i^T \mathbf{S}_{0,i}^{-1} \mathbf{K}_i + \left(\mathbf{S}_a^c \right)^{-1} \right)^{-1}. \tag{11}$$

We approximate the inverse of the Hessian using the Davidon–Fletcher–Powell (DFP) updating formula (Tarantola, 2004). This algorithm starts with an initial approximation of the inverse of the Hessian and combines it with gradients information from recent iterations of the minimization algorithm to update $\hat{\mathbf{S}}$. Since Eq. (7) optimizes the scaling factors but we need $\hat{\mathbf{S}}$ expressed in the flux space, it is necessary to rescale Eq. (9) to express the gradient of the cost function with respect to changes in the fluxes, $dJ/d\mathbf{x} = (dJ/d\mathbf{c})(d\mathbf{c}/d\mathbf{x})$, which yields

$$\nabla \mathbf{J}(\mathbf{x})_j = \nabla \mathbf{J}(\mathbf{c})_j / (\mathbf{x}_a)_j \tag{12}$$

for the gradient of the jth flux element. With this transformation, the update to estimate a posteriori covariance proceeds as follows. Let

$$\delta \mathbf{x}_n = \mathbf{x}_{n+1} - \mathbf{x}_n, \tag{13}$$
$$\delta \nabla \mathbf{J}(\mathbf{x})_n = \nabla \mathbf{J}(\mathbf{x})_{n+1} - \nabla \mathbf{J}(\mathbf{x})_n, \tag{14}$$

and then the inverse of the Hessian can be approximated by DFP updating formula as

$$\hat{\mathbf{S}}_{n+1} = \hat{\mathbf{S}}_n + \frac{\delta \mathbf{x}_n \delta \mathbf{x}_n^T}{(\delta \nabla \mathbf{J}(\mathbf{x})_n)^T \delta \mathbf{x}_n} - \frac{(\hat{\mathbf{S}}_n \delta \nabla \mathbf{J}(\mathbf{x})_n)(\hat{\mathbf{S}}_n \delta \nabla \mathbf{J}(\mathbf{x})_n)^T}{(\delta \nabla \mathbf{J}(\mathbf{x})_n)^T (\hat{\mathbf{S}}_n \delta \nabla \mathbf{J}(\mathbf{x})_n)}, \tag{15}$$

where n is the iteration number. The approach used here to estimate the inverse Hessian is similar to that of Muller and Stavrakou (2005).

2.5 Initial condition and model run schemes

The initial fields of the atmospheric CO_2 mixing ratio used are based on the results from an inversion analysis of flask observations from NOAA ESRL Carbon Cycle Co-operative Global Air Sampling Network sites and Environment Canada (EC) sampling
5 sites. GEOS-Chem was run from 1996 to the end of 2007 without assimilation to obtain a reasonable distribution of CO_2 in the troposphere and stratosphere, and then the flask observations were assimilated from January 2008 to the end of 2009. Comparison of the a posteriori CO_2 field in July 2009 with the GOSAT $X$$CO_2$ revealed the assimilated CO_2 fields were biased high relative to the GOSAT v2.9 data. To obtain initial conditions
10 for the $X$$CO_2$ inversions, we removed the global mean bias from the a posteriori CO_2 distribution from the flask inversion (hereafter referred to as "the original initial field") at 0 GMT on 1 July 2009. We scaled the original initial field by 0.99764, and 0.99734 to match the overall global $X$$CO_2$ values for XCO2_A, and XCO2_B, respectively, while we directly use the original initial field for XCO2_C. We carry out separate inversions for
15 each of these GOSAT $X$$CO_2$ datasets, which are referred to as RUN_A, RUN_B, and RUN_C. For evaluation of the inversion results with independent surface data, we start with the original initial field, rather than the adjusted fields, to simulate the a posteriori atmospheric CO_2. The $X$$CO_2$ inversion analyses were conducted from 1 July 2009, to 31 December 2010, however, we report here only the results for 2010 to avoid possible
20 discrepancies in the fluxes due to spin-up during the first 6 months.

3 Results

3.1 Optimized carbon fluxes and their uncertainties

Although our state vector includes emissions of CO_2 from fossil fuel combustion, when we report our a posteriori flux estimates, we remove the a priori fossil fuel estimate
25 from the reported total land flux. Also, although we optimize the GPP and TER fluxes

separately, we only report the net ecosystem exchange since the inferred GPP and TER fluxes will be highly correlated. Shown in Fig. 3 are annual fluxes for 2010 inferred from the GOSAT-ACOS XCO_2 data with the three different screening and correction schemes discussed in Sect. 2.1.1. The global total surface fluxes estimated from the three inversion analyses are similar: $-3.79\,\text{PgC}$, $-4.02\,\text{PgC}$, and $-4.35\,\text{PgC}$ for RUN_A, RUN_B, and RUN_C, respectively. Considering the $2.41 \pm 0.06\,\text{ppm}$ annual mean global carbon dioxide growth rate for 2010 (Conway and Tans, 2012) and the $8.90\,\text{PgC}$ a priori carbon emission from fossil fuel burning (including national fuel combustion and cement manufacturing ($8.542\,\text{PgC}$), international shipping ($0.192\,\text{PgC}$), and aviation ($0.162\,\text{PgC}$)) used for 2010, the global total surface flux should be $-3.78 \pm 0.13\,\text{PgC}$ ($-3.65 \sim -3.91\,\text{PgC}$), using the conversion factor of $2.124\,\text{PgC\,ppm}^{-1}$ to convert atmospheric CO_2 mixing ratio to PgC. The estimate from RUN_A is in this range, whereas the estimates from RUN_B and RUN_C exceed the lower bound with greater surface carbon uptake of 0.11, and $0.44\,\text{PgC}$. In terms of the land and ocean breakdown, we estimate that 2.16–$2.77\,\text{PgC}$ is fixed by the terrestrial biosphere, and 1.49–$1.63\,\text{PgC}$ is absorbed by the ocean in 2010, based on the three inversions. The estimates for the oceanic uptake vary less between the three inversions, which may be due to the fact that the oceanic flux estimates are dominated by the Takahashi et al. (2009) a priori fluxes because we did not use any atmospheric CO_2 observations over the ocean in the three inversions.

As can be seen in Fig. 3, the differences in the spatial distribution of the terrestrial carbon fluxes are large. Significant differences can be found between the inferred CO_2 fluxes from RUN_A and RUN_B, and between those from RUN_A and RUN_C, while the distribution obtained from RUN_B is relatively similar to that obtained from RUN_C. There are large differences, for example, over North America and South America (see Fig. 3). Carbon sources are inferred for the eastern US and southern Mexico from XCO2_A, whereas the eastern US region is found to be a sink, and the source in southern Mexico is much weaker with XCO2_B, and XCO2_C data. In South America, the strong carbon source in the eastern region inferred from the XCO2_A data

Title Page

Abstract | Introduction

Conclusions | References

Tables | Figures

|◄ | ►|

◄ | ►

Back | Close

Full Screen / Esc

Printer-friendly Version

Interactive Discussion

becomes much weaker when we use XCO2_B, and XCO2_C datasets. Although there are no grid boxes that are strong sources of CO_2 in RUN_C, the annual CO_2 source for tropical South America inferred from XCO2_C data is significantly greater than that inferred from XCO2_A, and XCO2_B data, as the number of inferred source grid cells is much greater in RUN_A than in RUN_B.

To help interpret our results, the monthly land fluxes are aggregated into the 11 TransCom land regions (Gurney et al., 2002) that are widely used. The total annual flux and the seasonal variations of the fluxes for each region are shown in Figs. 4 and 5, respectively. We estimate a sink for all four Eurasian regions (Europe, Boreal Eurasia, Temperate Eurasia, and Tropical Asia), as shown in Fig. 4, in all three inversion analyses. The estimated aggregated uptake for these regions is 3.69, 2.94, and 2.55 PgC from RUN_A, RUN_B and RUN_C, respectively. In the extratropics, the estimated fluxes are most similar across the three XCO_2 inversions for Boreal Eurasia and Temperate Eurasia, for which we estimated an annual CO_2 uptake in range of 0.49 to 0.68 PgC and 0.51 to 0.64 PgC, respectively. Their seasonal variations (Fig. 5) are also similar in the three inversions. We note that the a posteriori fluxes in Boreal Eurasia are close to the a priori used, reflecting, as discussed below, the lack of observational coverage in winter and with observations over the boreal region only available during May through September.

For Tropical Asia, the three XCO_2 inversions suggested a sink in the range of 0.69 to 1.32 PgC. The differences between inversions are manifested mainly in the region around the Indonesian islands (see Fig. 3), and between May to September (see Fig. 5). These differences amount to an increased uptake of about 0.63 PgC in the annual regional carbon budget (Fig. 4) in RUN_A compared to RUN_C.

The largest differences in the inferred fluxes for the three XCO_2 inversions were obtained for Temperate North America and Temperate South America. The differences in the estimated fluxes between RUN_A and RUN_C were 1.02 and 0.96 PgC for Temperate North American and Temperate South American, respectively. The differences in the estimated fluxes between RUN_B and RUN_C were smaller. The fluxes inferred

for Boreal North America also varied significantly between the three inversions, but the absolute magnitude of the differences was small. We also conducted an inversion analysis of the surface flask data and the differences between the fluxes inferred from the flask data and those based on the XCO$_2$ for Temperate North American is striking. With XCO2_A we estimated a source of about 0.5 PgC for Temperate North America, whereas with the flask data we estimated a sink of about 0.7 PgC (Fig. 4). Examination of the seasonal variations in Fig. 5 shows that there are significant differences among the three inversions in the timing and extent of the uptake of CO$_2$ in July, August, and September in Boreal North America. In Temperate North America the monthly mean uptake in RUN_A is systematically smaller from May through September than in the other two runs. In Temperate South America, CO$_2$ uptake during the growing season in RUN_A is much less than in the other two runs, especially between January–April. Considering the spatial distribution, these differences in Temperate South America are mostly caused by the stronger uptake in RUN_C and RUN_B than in RUN_A in the eastern part of this region.

The posterior errors derived from the 4D-Var inversion using Eq. (15) have been aggregated to the TransCom regions. The uncertainties of the land fluxes and the flux for each month are given in Fig. 5. These uncertainties can be further used to calculate the uncertainty reduction percentage (Deng et al., 2007), given as

$$U_r = \left(1 - \frac{\sigma}{\sigma_a}\right) \times 100\,\%. \tag{16}$$

where σ and σ_a are the a posteriori and a priori uncertainties, respectively. The uncertainty reduction obtained for RUN_A is shown in Fig. 6. The uncertainty reduction on the regional flux estimates varies significantly from region to region. The minimum uncertainty reductions can be as small as less than 1 % for the three northern high-latitude regions (Boreal North America, Europe, and Boreal Eurasia) during winter months, which, as we will discuss below, is due to the scarcity of XCO$_2$ observations in these regions in winter. The largest uncertainty reduction (exceeding 35 %) for the regional

flux estimates was obtained for the fluxes inferred for Temperate North America, the two South American regions, and the two African regions. The largest uncertainty reduction that we obtained was about 50 % for Tropical South America. We note that these estimates of uncertainty reduction depend largely on our assumed a priori uncertainty. Comparison of the monthly mean fluxes in Fig. 5 indicates the differences in the flux estimates inferred from the different datasets is larger than the estimated a posteriori uncertainties, suggesting that it is likely that we have underestimated the observation errors. Neglect of spatial and temporal correlations in the a priori error covariance matrix would also result in an underestimate of the a posteriori errors and, consequently, an overestimate of the uncertainty reduction. Clearly, the estimated uncertainty reduction depends strongly on the specification of the observation and a priori error covariance matrix, which are difficult to characterize. Therefore, in our interpretation of the uncertainty reduction in Sect. 4 we will focus on the relative uncertainty reduction between the different regions and not on the magnitude of the error reduction.

3.2 Evaluation of the inversions

3.2.1 Comparison with GOSAT XCO_2

The objective of the inversion analysis, as described by Eq. (7), is to optimize the fluxes to minimize the mismatch between the model and observations. One way of assessing the success of the inversion is by the degree to which the a posteriori CO_2 matches the observations. Shown in Fig. 7 are the model and GOSAT XCO_2 differences for RUN_A. It shows that the distribution of the model and observations differences is approximately Gaussian. As an indication of the overall inversion performance, the mean global bias is reduced from 2.72 ppm to 0.04 ppm, while the 1σ spread is also reduced from 2.18 ppm to 1.65 ppm. On the hemispheric scale, the residual bias is smaller in the Northern Hemisphere (NH) than in the Southern Hemisphere (SH). In the NH, the mean bias is 0.01 ppm (reduced from 3.21 ppm in the a priori, with a decrease in the standard deviation from 2.24 ppm to 1.81 ppm), whereas in the SH, the mean

bias is 0.08 ppm (reduced from 2.02 ppm, with a decrease in the standard deviation from 1.88 ppm to 1.39 ppm). While the mean biases have been reduced satisfactorily in both hemispheres, the larger standard deviation obtained in the NH may reflect the difficulty of reliably capturing the greater biospheric sources and sinks in the NH.

5   We also examined the seasonality of the residual bias, focusing on April–September as the growing season and October–March as the non-growing season in the NH, and vice versa for the SH, to broadly reflect the hemispheric biosphere carbon cycle dynamics. During the growing season, the residual biases were 0.00 ppm and 0.03 ppm for the NH and SH, respectively. During the non-growing season, the biases were 0.02

10   and 0.09 ppm, for the NH and SH, respectively. We believe that the relatively small biases of 0.03 ppm and 0.00 ppm obtained for the SH and NH, respectively, during their growing season is due to the fact that more XCO$_2$ data are available to constrain the inversion analysis during these periods. One common feature among the four cases examined is that the standard deviations of the a posteriori biases are greater during

15   the growing season on both hemispheres than during the non-growing season, indicating that larger uncertainties may be related to simulating the summertime drawdown of atmospheric CO$_2$.

3.2.2   Comparison with independent observations

Flask observations

20   Flask observations provide the research community with highly accurate and precise atmospheric CO$_2$ measurements that are often used to calibrate new atmospheric CO$_2$ measurements. We use here flask observations from the 78 observing sites shown in Fig. 2, corresponding to 3016 flask observations in 2010, to evaluate the a posteriori CO$_2$ fluxes. We sampled the modeled CO$_2$ distribution at the appropriate measurement

25   location and time (to within one hour of the measurement time). Using the a posteriori results from the three GOSAT XCO$_2$ inversions, we estimated a mean difference of −0.88 ppm, −0.99 ppm, and 0.01 ppm relative to the 3016 flask observations in 2010.

These mean differences for RUN_A and RUN_B could be due to the overall systematic errors transferred from the XCO_2 data when we adjusted the initial CO_2 distribution in the inversion to remove the mean mismatch with the GOSAT data. Therefore, it would be inappropriate to directly compare the modeled a posteriori mixing ratios against real flask observations to evaluate our flux estimates. Instead we simulated the a posteriori CO_2 mixing ratios, based on the optimal CO_2 flux estimates, starting from the original initial CO_2 field (which as discussed in Sect. 2.5, was based on an assimilation of the surface data).

Figure 8 shows the observed and simulated CO_2 time series at four flask sites: ALT (Alert, Nunavut, Canada), MLO (Mauna Loa, Hawaii, USA), GMI (Mariana Islands, Guam), and CGO (Cape Grim, Tasmania, Australia). Because we assumed a balanced biosphere (with zero annual net uptake) for our a priori fluxes, the a priori CO_2 distribution significantly overestimates the observations at the flask sites by the end of 2010. The a priori overestimate largely reflects the well-established secular increase in atmospheric CO_2 due to anthropogenic emissions, and the inversion successfully corrects for it. In general, the seasonal variation of the observed atmospheric CO_2 time series has been satisfactorily simulated using the a posteriori fluxes, optimized from ACOS GOSAT XCO_2 data, considering the spatial and temporal resolution of the model. We intentionally started with a poor a priori flux to better assess the ability of the observations to constrain the flux estimates. The mean, the standard deviation (STDV), and the mean absolute value (MAV) of the mismatch between the a posteriori model and observations are listed in Table 2. For ALT, MLO, and GMI, the mean differences are small, much less than 1 ppm. For CGO, however, the a posteriori CO_2 is biased low by slightly more than 1 ppm for RUN_A and RUN_B, while the bias was significantly reduced to −0.68 for RUN_C. For all 78 flask sites, the mean of the model-observation mismatch is 0.02 ppm, 0.05 ppm, and 0.01 ppm for RUN_A, RUN_B, and RUN_C, respectively, indicating that, on average, the observations have been simulated well with the optimal fluxes. The underestimate at CGO is not unique to that station. We find that the a posteriori fluxes underestimate CO_2 at the surface sites across the southern

Full Screen / Esc

Printer-friendly Version

Interactive Discussion

extratropics. However, the magnitude of the underestimate is highly variable. At Palmer Station, Antarctica (PSA), for example, the mean difference is only −0.21 ppm and the MAV is 0.21 (not shown) in RUN_A, compared to −1.18 ppm for the mean difference and 1.18 for the MAV at CGO. Examination of the mean and MAV suggests that RUN_C provides a relatively better overall simulation compared with observations from all 78 sites.

TCCON observations

We evaluated the a posteriori flux estimates using TCCON by comparing the observations with the a posteriori atmospheric CO_2 mixing ratios that were produced with the model simulation initialized with the original initial CO_2 field. As with the flask data, the model was sampled at the observation location and time (to within one hour). To compare with the TCCON XCO_2, the modelled CO_2 concentrations are mapped to the TCCON 71 vertical layers and then transformed using the a priori profile and average kernel extracted from the TCCON dataset. Finally, the XCO_2 values are calculated using the approach of Wunch et al. (2011). Figure 9 shows the observed and modeled XCO_2 time series at four selected sites: (1) Lamont, USA, (2) Sodankylä, Finland, (3) Izana, Tenerife, and (4) Wollongong, Australia. The a posteriori CO_2 field reproduced well the observed seasonal variations at these four sites. However, the model underestimated the XCO_2 at Lamont and Izana in summer (between days 150–250), and overestimated it at Sodankylä and Wollongong throughout 2010. Using the scaled initial field, our calculation shows that the means of the mismatches between the modeled a posteriori hourly atmospheric CO_2 mixing ratios and the observations at 13 TCCON sites in 2010 are −0.79 ppm, −1.27 ppm, and 0.06 ppm for all three inversions, respectively.

The mean model and observation mismatch, the standard deviation (STDV), and the mean absolute value (MAV) of the differences for all 13 TCCON sites are given in Table 3. The mean mismatch for all 13 sites is 0.16 ppm, −0.23 ppm, and −0.30 ppm for RUN_A, RUN_B, and RUN_C, respectively. On average, as indicated in Table 3, the

XCO_2 at Park Falls, Orleans, Karlsruhe, Bialystok, Darwin, and Lauder are well simulated by the a posteriori fluxes from all three inversions, with mean biases that are less than or equal to 0.70 ppm. RUN_B produced the best a posteriori CO_2 compared to the TCCON observations in Southern Hemisphere (including Darwin, Wollongong, and Lauder) in terms of both the mean and the MAV, while RUN_A produced the best a posteriori CO_2 comparing with northern subtropical (Lamont, and Izana) observations. For the northern sites, no single inversion consistently agrees well with all the observations, however, RUN_B and RUN_C generally produced better a posteriori CO_2 fields relative to the observations. Considering all 13 sites, RUN_C has the least absolute mean bias (0.06 ppm) and the least MAV (0.91 ppm). It also has the strongest correlation (r^2 = 0.80) with the observed XCO_2 at all 13 sites.

HIPPO aircraft measurements

As discussed in Sect. 2.1.4, we compare our a posteriori CO_2 fields with the 10 s averaged HIPPO-3 data. At this temporal resolution, the HIPPO data will reflect CO_2 on spatial scales smaller than the model resolution. We do not average the HIPPO data onto the model grid, so the differences between the model and the observations will also reflect representativeness errors associated with the coarse model grid. Listed in Table 4 are the mean differences, the standard deviation, and the mean absolute value of model and observation mismatch for all 24 303 HIPPO-3 observations. In general, the results from the three inversions are not significantly different from each other. We estimated mean differences of −0.07 ppm, −0.08 ppm, and −0.17 ppm for RUN_A, RUN_B, and RUN_C, respectively. In contrast, using the scaled initial field results in mean differences between the a posteriori CO_2 and the HIPPO data of −1.01 ppm, −1.12 ppm, and −0.17 ppm, respectively, reflecting the global mean bias in the initial conditions used for the XCO_2 inversions.

To better evaluate the performance of the inversion analyses, we also compared the a posteriori CO_2 to the HIPPO data only between 1000 m to 5000 m in altitude. Figure 10 shows three sets of plots comparing simulated HIPPO observations with

optimal surface fluxes from our three inversions with the HIPPO-3 observations. As our model is sampled with a temporal resolution of one hour, and the spatial resolution of the model is coarse ($4° \times 5°$), the modeled CO_2 does not reproduce much of the detailed structure seen in the observations. The a posteriori simulations based on the optimal fluxes from RUN_B deviate from the observation the most in the southern high-latitudes. For example, the mean differences in the southern high latitudes, $70°$ S–$45°$ S can be as large as -0.92 ppm. However, the simulations based on a posteriori fluxes from RUN_B are less biased relative to the observations in the tropics and the Northern Hemisphere. The a posteriori simulation based on RUN_C has the smallest bias in the Southern Hemisphere between $15°$ S to $70°$ S, but the largest bias in the tropics ($15°$ S to $15°$ N). The posterior CO_2 from RUN_A deviate from the observations the most in the Northern Hemisphere ($15°$ N to $80°$ N). Overall, the simulations compare well to the HIPPO data. The correlation between the a posteriori simulations and the observations are $r^2 = 0.96$ for all three inversion runs.

Eddy covariance-derived product

In Fig. 11 we compare our inferred fluxes for Temperate North America and Europe with the MPI-BGC fluxes (Jung et al., 2011), which are empirically derived from eddy covariance measurements. We focus on North America and Europe for this comparison since the density of eddy covariance towers is greatest in these regions. For Temperate North America, the MPI-BGC fluxes suggest weaker uptake in May and June than inferred from RUN_B, whereas the June MPI-BGC flux is in agreement with the estimates in RUN_A and RUN_C. However, for July – September the MPI-BGC data product suggests greater uptake than the three XCO_2 inversions and the flask inversion. For Europe, the MPI-BGC data are generally consistent with the results of the inversions. The major discrepancy between the three XCO_2 inversions and the MPI-BGC data occurs in May, when all three inversions suggested greater uptake of CO_2. In contrast, the flask inversion suggested slightly weaker uptake. Wintertime fluxes in the inversions tend to be larger sources than that from MPI-BGC in Europe.

4   Discussion

4.1   Regional flux estimates

Terrestrial ecosystem (biosphere) models often underestimate the seasonal amplitude of CO_2 in the Northern Hemisphere (Randerson et al., 2009), and inversion analyses
5 that employ these terrestrial ecosystem models to provide a priori flux estimates underestimate the CO_2 seasonal amplitude by 1 to 2 ppm (Basu et al., 2011; Peters et al., 2010). In this study, we used the annual balanced, 3 hourly terrestrial ecosystem fluxes as described by Deng and Chen (2011), which also produced a weak seasonal cycle in the a priori CO_2 fields. However, as shown in Figs. 8 and 9, the a posteriori simula-
10 tions reproduced well the amplitude of the seasonal cycle measured at the flask and TCCON sites. This improvement in the modeled seasonal cycle could be attributed to the good spatial coverage of the GOSAT observations during the growing season. This correction in the modeled seasonal cycle is reflected in the significantly greater uptake of CO_2 during the growing season obtained for the regions in the extratropical Northern
15 Hemisphere (Fig. 5).

Using the ACOS XCO$_2$ data screened and bias corrected by the three different approaches produced significantly different surface fluxes for regions such as Boreal North America, Temperate North America, and Temperate South America. The sensitivity of the inferred flux estimates for Boreal North America is not surprising since
20 the GOSAT observational coverage is limited at high latitudes over North America. The Temperate North America region has been described as a sink in previous inversions using flask observations of atmosphere CO_2 (Deng and Chen, 2011; Gurney et al., 2004; Peters et al., 2007; Rayner et al., 2008; Deng et al., 2007). Here we estimated the region to be a significant source in RUN_A, but a weak sink in RUN_B and
25 a strong sink in RUN_C. Our flask inversion suggested a stronger sink for the region. The differences are mostly caused by the uptake in the growing season. All three XCO$_2$ inversions and the flask inversion estimated peak uptake of CO_2 in Temperate North America in June, with the flask and RUN_A inversions producing similar estimates of

the June uptake. In contrast, in RUN_B and RUN_C, we estimated stronger uptake in June. Unlike the flask inversion, all the XCO_2 inversions produced much weaker uptake in July compared to June. Comparison with the TCCON observations at Lamont from day 120–250 (Fig. 9) shows the strong negative bias for RUN_B and RUN_C, which
5 could indicate that the stronger uptake inferred in these inversions for Temperate North America represent an overestimate of the actual sink during the growing season (in the absence of compensatory changes in the flux from other regions). Surface flask observations, for example, at the KEY site and inland at NWR and SGP (not shown), also suggest that the summertime sinks estimated in RUN_B and RUN_C for Temperate
10 North America were overestimated. A weak sink for Temperate North America is possible for 2010 as a result of the cold spring and hot and dry summer in the southeast US during 2010 (Blunden et al., 2011). In addition, fire emissions in British Columbia, Canada, in July would have further reduced the net uptake of CO_2 from Temperate North America in 2010. Indeed, these could be responsible for the strong decrease in
15 uptake in the three XCO_2 inversions in July.

For Temperate South America, we estimated a strong source in RUN_A, a weak source in RUN_B, and a strong sink in RUN_C (Fig. 4). As shown in Fig. 5, these differences are largely due to the estimated uptake during January to May. For these months, RUN_B and RUN_C suggest greater uptake than RUN_A, with sink estimates
20 comparable to those inferred from the flask data and similar to the a priori fluxes. Comparison with the flask data from the PSA flask station at the South Pole (not shown), reveals that the a posteriori CO_2 concentrations from all three XCO_2 inversions underestimate the observed CO_2 concentrations, with the underestimate being greater for RUN_B during the first half of 2010. However, this is not the case for RUN_C though the
25 inferred fluxes from XCO2_C are almost identical to those from XCO2_B for the same period. A possible explanation is that lower uptake in Australia, inferred from XCO2_C, could in part compensate for the inferred fluxes from Temperate South America. Comparison with the HIPPO-3 data (see Fig. 10) shows that the a posteriori CO_2 fields from RUN_B are also more negatively biased relative to the independent aircraft data

than those from RUN_A and RUN_C, suggesting the need for a weaker uptake or large emissions of CO_2 in the southern extratropics in early 2010.

4.2 Regional sensitivity analysis

The uncertainty reductions on the regional flux estimates, as shown in Fig. 6, vary considerably both in space (regions) and time (seasons). The largest uncertainty reduction (about 50 %) was for the flux estimates from Tropical South America. The other regions with large uncertainty reduction are Temperate South America, Northern and Southern Africa, and Temperate North America. The large uncertainty reduction on the flux estimates in the tropics is not surprising given the observational coverage of GOSAT. We note here that interpretation of the uncertainty reduction should be taken with care, as it depends on the magnitude of the assumed a priori uncertainty and observation errors. Furthermore, we used a scheme in which the a priori uncertainties were proportional to the a priori flux estimates, so regions with large absolute a priori fluxes (such as South American Tropical) would have large a priori uncertainties and, subsequently, large uncertainty reductions, whereas regions with small absolute a priori fluxes could have small uncertainty reductions. Therefore, the uncertainty reductions should be used only as a metric to assess the relative impact of the observation constraints on the regional flux estimates.

In the northern extratropics, the largest uncertainty reduction obtained was for Temperate North America. Examination of the uncertainty reduction of the monthly mean fluxes in 2010 revealed that the uncertainty reduction in the flux estimate for Temperate North America was at a maximum (about 35 %) in April, with comparably large uncertainty reduction in October. The smallest uncertainty reduction was for December 2010, due to the smaller number of observations used for quantifying the December fluxes compared to previous months (since the assimilation period ended on 31 December 2010). The other extratropical regions with large uncertainty reduction are Europe and Boreal Eurasia. For both regions the uncertainty reduction on the flux

estimates was small in winter and peaked at about 20 % and 25 % in May and July, respectively.

To explain the relative differences in the uncertainty reduction for Europe and North America, for example, we constructed the regional Jacobians, which give the sensitivity of the modeled XCO_2 to the regional flux estimates. The Jacobian is obtained by taking the derivative of the observation operator Eq. (8) with respect to the emissions, which gives

$$\frac{dXCO_2^m}{dx} = \sum_j \mathbf{h}_j \mathbf{a}_{CO_2,j} \left(\frac{dH(x)}{dx} \right)_j \tag{17}$$

The derivative $dH(x)/dx$ is available from the adjoint sensitivities, but we choose here to estimate them using separate tracers for each of the main continental regions in the northern extratropics. With this construction of the sensitivities it will be easier to interpret our results in the context of previously published TransCom inversions. We specify a 1 Pg C source for North America, Europe, and Asia, using the distribution of CO_2 fluxes shown in Fig. 12. This 1 Pg C source of CO_2 was emitted over a period of one month for each region, but the resulting tracer distribution was simulated for three months. The sensitivities were calculated using Eq. (17), by sampling the tracer distribution at the GOSAT observation locations and time (to within an hour) and applying the GOSAT averaging kernels. The sensitivities for January 2010 XCO_2 to fluxes in January are shown in Fig. 13. Over Europe there is weak sensitivity to European fluxes due to the limited observational coverage. In contrast, there is greater sensitivity to North American emissions due to the good coverage over the United States. This accounts for the greater wintertime uncertainty reduction in flux estimates from North America than from those from Europe. In April, there is significantly greater observational coverage over Europe and as a result (Fig. 13), there is strong sensitivity of the April XCO_2 over Eurasia to European fluxes in April. In May, as a result of transport, the sensitivities of the modeled XCO_2 to April fluxes have been reduced relative to the sensitivities in April (Fig. 14). We find that European and North American fluxes in

April most strongly influence XCO_2 values across Eurasia in May. The sensitivity of the Eurasia XCO_2 to North American fluxes is due to the efficient transport of air from the North American boundary layer across the Atlantic to Europe in the free troposphere and in the boundary layer (Li et al., 2002).

5   To help interpret the regional sensitivities we calculated the transit times of air from the boundary layer of North America, Europe, and Asia to the receptor regions shown in Fig. 12. Instead of emitting the CO_2 for the regional tracers over a period of one month, we emitted the $1\,Pg\,C$ from each region within one day to simulate the release of each tracer that is a delta function in time, producing a tracer distribution that is anal-

10   ogous to an age spectrum (Hall and Plumb, 1994; Holzer and Hall, 2008). Figure 15 shows the transit times to the middle troposphere over the receptor regions in Fig. 12 for June 2010 conditions. The distribution of transit times shown in Fig. 15 was obtained from the release of the tracers on 1 June 2010, but we also examined the transit times for tracers released in 10 day intervals in June and found that the changing syn-

15   optic conditions in June did not significantly change the distribution. Furthermore, the distribution of transit time is consistent with those shown by Holzer and Hall (2008). As expected, over each continental region, transport of CO_2 from the boundary layer to the middle troposphere peaks on the timescale of a few days. Figure 15 shows the rapid transport of North American air across the Atlantic. Within 15 days, North American

20   CO_2 is transported across to Europe and Siberia. This suggests that, in the context of the inversion, on timescales of one to two weeks, North American flux estimates are influenced by XCO_2 observations across North America and Eurasia. In contrast, over East Asia and the Pacific, the North American signal is well mixed into the background.

     Examination of Fig. 15 reveals that the transport of European CO_2 out of Europe

25   and Siberia is sufficiently long that outside of these regions the European signal is also well mixed into the background. This suggests that European flux estimates will be influenced mainly by observations over Europe and Siberia, on timescales of about one week. As a result, the European flux estimates will be sensitive mainly to biases in the XCO_2 data over Eurasia, whereas North American flux estimates will be sensitive to

regional biases in the data over North America as well as over Eurasia. This greater influence of long-range transport on the North American fluxes suggests that North American flux estimates should be more sensitive to model transport errors than European flux estimates. However, the actual impact on the estimated fluxes will depend on the relative magnitudes of the North American and European fluxes.

The timescale for transport across the Pacific Ocean is longer than for transport across the Atlantic Ocean; however, Fig. 15 shows that the Asian signal remains above the background across the Pacific and over North America. Despite this influence of long-range transport on the Asian fluxes, our inversion exhibited low sensitivity to Asian CO_2 fluxes due to the absence of ocean observations and the limited GOSAT observational coverage over East Asia, as a result of cloud cover. This suggests that incorporating ocean observation over the mid-latitude and northern Pacific should produce greater constraints on the Asian fluxes.

5 Conclusions

We have conducted inversion analyses using three different sets of the NASA ACOS GOSAT XCO_2 b2.9 and b2.10 data to quantify regional sources and sinks of atmospheric CO_2. We found that the seasonal variations of the inferred global fluxes were consistent across the three XCO_2 inversions. The inversions significantly increased the uptake in the northern extratropics to correct for the underestimate of the seasonal cycle in our a priori fluxes. The a posteriori CO_2 was in better agreement with independent TCCON, surface flask, and HIPPO aircraft observations. On regional spatial scales, we found that the flux estimates were sensitive to the treatment of the residual bias in the GOSAT XCO_2 data. The largest differences obtained were for Temperate North America and Temperate South America, for which the largest spread between the inversions was 1.02 Pg C and 0.96 Pg C, respectively. In the case of Temperature North America, one inversion suggested a strong source (RUN_A), whereas the second and third inversion produced a weak (RUN_B) and strong sink (RUN_C), respectively. However,

inversion of the surface flask data produced an even stronger sink for Temperate North America than was inferred from the GOSAT data. We found that the flux estimates from Boreal Eurasia, Temperate Eurasia, and Europe were generally consistent across the three XCO$_2$ inversions. Comparison of the a posteriori flux estimates with the MPI-BGC eddy covariance flux-based product showed that the inferred European fluxes were consistent with the eddy covariance flux product, whereas the North American fluxes were offset by ∼ 1 month and a weaker sink.

The XCO$_2$ inversions produced the largest uncertainty reduction on the flux estimates for South America and Africa, with the greatest uncertainty reduction on the flux estimates for Tropical South America. In the northern extratropics, the largest uncertainty reduction was for the Temperate North American flux estimates, which our sensitivity analysis suggests is due to the fact that North American flux estimates are influenced by observations over Eurasia on time scales of one to two weeks as a result of the long-range transport of CO$_2$ from North America. In contrast, European flux estimates are influenced mainly by observations on the Eurasian continent on time scales of less than a week. A consequence of this greater influence of long-range transport is that North American flux estimates should be more sensitive to regionally varying biases in the observations and to model transport errors. The low sensitivity of the European flux estimates to observations outside of Eurasia could explain why the inferred European flux estimates are more robust across the three different XCO$_2$ datasets.

We found that the GOSAT observational coverage is a challenge for the inversion. The greater sensitivity to North American fluxes than European and Asia fluxes, for example, is due to the lack of observations over Eurasia in winter and over eastern and southern Asia in summer. Since the observations over Eurasia are restricted to summer, it is unclear how reliable are the European flux estimates, despite the fact that they are robust across the three XCO$_2$ inversions. Increased wintertime observational coverage in Eurasia is critical for better quantifying the seasonal variation in the extratropical sources and sinks of CO$_2$. The use of M-gain GOSAT data over North Africa would also provide additional constraints on European flux estimates. A particular con-

cern is the low sensitivity to Temperate Asian fluxes in the inversion. During the growing season, the data density is low over Temperate Asia as a result of cloud cover from the Asian monsoon. The use of ocean observations over the Pacific would help capture the Asia outflow and better quantify the Asia fluxes. Similarly, observations over the North
5　Atlantic would provide useful information on North America CO_2 fluxes. The ocean glint data from GOSAT could be useful in this context, but these data are mainly in the tropics and subtropics. Incorporating the thermal infrared (TIR) GOSAT CO_2 retrievals with the XCO_2 data, could better capture the continental outflow and provide greater constraints on the Asia, North American, and tropical fluxes, from regions such as the
10　Amazon, where persistent cloud cover is a challenge for the GOSAT retrievals.

Although the global flux estimates inferred in the different inversion analyses presented here were robust, the regional flux estimates were less reliable. In our analyses, we focused on fixed regions, as defined by TransCom, to facilitate comparison with previous inversion analyses in the literature. However, the actual regional scales
15　on which the inversion analyses can constrain the flux estimates will depend on the observational coverage, the observational error, the specified a priori flux errors, and the changing atmospheric transport patterns. An objective approach is clearly needed to determine the minimum spatial scales at which the fluxes can be reliably quantified. There is also critical need for additional independent data to better evaluate the
20　inferred fluxes. Despite the large spread in the flux estimates obtained for regions such as Temperate North America, Tropical South America, and Temperate South America, we found that the different inversion analyses reproduced well the independent atmospheric CO_2 data and were similar in their agreement with the data (with mean differences typically less than 0.5 ppm). This raises the issue as to how we should em-
25　ploy the existing datasets, and what additional observations are needed, to provide a more stringent evaluation of the inferred flux estimates.

Inferring CO₂ fluxes from GOSAT *X*CO₂

F. Deng et al.

References

Andres, R. J., Gregg, J. S., Losey, L., Marland, G., and Boden, T. A.: Monthly, global emissions of carbon dioxide from fossil fuel consumption, Tellus B, 63, 309–327, doi:10.1111/j.1600-0889.2011.00530.x, 2011.

Baker, D. F., Doney, S. C., and Schimel, D. S.: Variational data assimilation for atmospheric CO_2, Tellus B, 58, 359–365, doi:10.1111/j.1600-0889.2006.00218.x, 2006a.

Baker, D. F., Law, R. M., Gurney, K. R., Rayner, P., Peylin, P., Denning, A. S., Bousquet, P., Bruhwiler, L., Chen, Y. H., Ciais, P., Fung, I. Y., Heimann, M., John, J., Maki, T., Maksyutov, S., Masarie, K., Prather, M., Pak, B., Taguchi, S., and Zhu, Z.: TransCom 3 inversion intercomparison: impact of transport model errors on the interannual variability of regional CO_2 fluxes, 1988–2003, Global Biogeochem. Cy., 20, GB1002, doi:10.1029/2004gb002439, 2006b.

Baldocchi, D.: Turner review no. 15. "Breathing" of the terrestrial biosphere: lessons learned from a global network of carbon dioxide flux measurement systems, Aust. J. Bot., 56, 1–26, doi:10.1071/BT07151, 2008.

Baldocchi, D., Falge, E., Gu, L., Olson, R., Hollinger, D., Running, S., Anthoni, P., Bern-
hofer, C., Davis, K., Evans, R., Fuentes, J., Goldstein, A., Katul, G., Law, B., Lee, X.,
Malhi, Y., Meyers, T., Munger, W., Oechel, W., Paw, K. T., Pilegaard, K., Schmid, H. P.,
Valentini, R., Verma, S., Vesala, T., Wilson, K., and Wofsy, S.: FLUXNET: A new tool to
study the temporal and spatial variability of ecosystem-scale carbon dioxide, water va-
por, and energy flux densities, B. Am. Meteorol. Soc., 82, 2415–2434, doi:10.1175/1520-
0477(2001)082<2415:FANTTS>2.3.CO;2, 2001.
Basu, S., Houweling, S., Peters, W., Sweeney, C., Machida, T., Maksyutov, S., Patra, P. K.,
Saito, R., Chevallier, F., Niwa, Y., Matsueda, H., and Sawa, Y.: The seasonal cycle amplitude
of total column CO_2: factors behind the model-observation mismatch, J. Geophys. Res., 116,
D23306, doi:10.1029/2011jd016124, 2011.
Basu, S., Guerlet, S., Butz, A., Houweling, S., Hasekamp, O., Aben, I., Krummel, P., Steele, P.,
Langenfelds, R., Torn, M., Biraud, S., Stephens, B., Andrews, A., and Worthy, D.: Global CO_2
fluxes estimated from GOSAT retrievals of total column CO_2, Atmos. Chem. Phys. Discuss.,
13, 4535–4600, doi:10.5194/acpd-13-4535-2013, 2013.
Blunden, J., Arndt, D. S., and Baringer, M. O.: State of the climate in 2010, B. Am. Meteorol.
Soc., 92, S1–S236, doi:10.1175/1520-0477-92.6.s1, 2011.
Bruhwiler, L. M. P., Michalak, A. M., and Tans, P. P.: Spatial and temporal resolution of carbon
flux estimates for 1983–2002, Biogeosciences, 8, 1309–1331, doi:10.5194/bg-8-1309-2011,
2011.
Canadell, J. G., Le Quéré, C., Raupach, M. R., Field, C. B., Buitenhuis, E. T., Ciais, P., Con-
way, T. J., Gillett, N. P., Houghton, R. A., and Marland, G.: Contributions to accelerating
atmospheric CO_2 growth from economic activity, carbon intensity, and efficiency of natural
sinks, P. Natl. Acad. Sci. USA, 104, 18866–18870, doi:10.1073/pnas.0702737104, 2007.
Chen, J. M., Liu, J., Cihlar, J., and Goulden, M. L.: Daily canopy photosynthesis model through
temporal and spatial scaling for remote sensing applications, Ecol. Model., 124, 99–119,
1999.
Chevallier, F., Bréon, F.-M., and Rayner, P. J.: Contribution of the orbiting carbon observatory to
the estimation of CO_2 sources and sinks: theoretical study in a variational data assimilation
framework, J. Geophys. Res., 112, D09307, doi:10.1029/2006jd007375, 2007.
Chevallier, F., Maksyutov, S., Bousquet, P., Bréon, F.-M., Saito, R., Yoshida, Y., and Yokota, T.:
On the accuracy of the CO_2 surface fluxes to be estimated from the GOSAT observations,
Geophys. Res. Lett., 36, L19807, doi:10.1029/2009gl040108, 2009.

Title Page

Abstract | Introduction

Conclusions | References

Tables | Figures

|◄ | ►|

◄ | ►

Back | Close

Full Screen / Esc

Printer-friendly Version

Interactive Discussion

Conway, T. J. and Tans, P.: NOAA/ESRL, available at: http://www.esrl.noaa.gov/gmd/ccgg/trends/, last access: December 20, 2012, 2012.

Conway, T. J., Lang, P. M., and Masarie, K. A.: Atmospheric Carbon Dioxide Dry Air Mole Fractions from the NOAA ESRL Carbon Cycle Cooperative Global Air Sampling Network, 1968–2010, version: 14 October 2011, availabe at: ftp://ftp.cmdl.noaa.gov/ccg/co2/flask/event/, last access: December 12, 2011, 2011.

Corbett, J. J.: Considering alternative input parameters in an activity-based ship fuel consumption and emissions model: reply to comment by Øyvind Endresen et al. on "Updated emissions from ocean shipping", J. Geophys. Res., 109, D23303, doi:10.1029/2004jd005030, 2004.

Corbett, J. J. and Koehler, H. W.: Updated emissions from ocean shipping, J. Geophys. Res., 108, 4650–4666, doi:10.1029/2003jd003751, 2003.

Deng, F. and Chen, J. M.: Recent global CO_2 flux inferred from atmospheric CO_2 observations and its regional analyses, Biogeosciences, 8, 3263–3281, doi:10.5194/bg-8-3263-2011, 2011.

Deng, F., Chen, J. M., Plummer, S., Chen, M., and Pisek, J.: Algorithm for global leaf area index retrieval using satellite imagery, IEEE T. Geosci. Remote, 44, 2219–2229, doi:10.1109/tgrs.2006.872100, 2006.

Deng, F., Chen, J. M., Ishizawa, M., Yuen, C.-W., Mo, G., Higuchi, K., Chan, D., and Maksyutov, S.: Global monthly CO_2 flux inversion with a focus over North America, Tellus B, 59, 179–190, doi:10.1111/j.1600-0889.2006.00235.x, 2007.

Deutscher, N. M., Griffith, D. W. T., Bryant, G. W., Wennberg, P. O., Toon, G. C., Washenfelder, R. A., Keppel-Aleks, G., Wunch, D., Yavin, Y., Allen, N. T., Blavier, J.-F., Jiménez, R., Daube, B. C., Bright, A. V., Matross, D. M., Wofsy, S. C., and Park, S.: Total column CO_2 measurements at Darwin, Australia – site description and calibration against in situ aircraft profiles, Atmos. Meas. Tech., 3, 947–958, doi:10.5194/amt-3-947-2010, 2010.

Endresen, Ø., Sørgård, E., Bakke, J., and Isaksen, I. S. A.: Substantiation of a lower estimate for the bunker inventory: comment on "Updated emissions from ocean shipping" by Corbett, J. J. and Koehler, H. W., J. Geophys. Res., 109, D23302, doi:10.1029/2004jd004853, 2004.

Endresen, Ø., Sørgård, E., Behrens, H. L., Brett, P. O., and Isaksen, I. S. A.: A historical reconstruction of ships' fuel consumption and emissions, J. Geophys. Res., 112, D12301, doi:10.1029/2006jd007630, 2007.

Title Page

Abstract | Introduction

Conclusions | References

Tables | Figures

◄◄ | ►►

◄ | ►

Back | Close

Full Screen / Esc

Printer-friendly Version

Interactive Discussion

Enting, I. G., Trudinger, C. M., and Francey, R. J.: A synthesis inversion of the concentration and δ^{13} C of atmospheric CO_2, Tellus B, 47, 35–52, 1995.

Fan, S., Gloor, M., Mahlman, J., Pacala, S., Sarmiento, J., Takahashi, T., and Tans, P.: A large terrestrial carbon sink in North America implied by atmospheric and oceanic carbon dioxide data and models, Science, 282, 442–446, doi:10.1126/science.282.5388.442, 1998.

Gurney, K. R., Law, R. M., Denning, A. S., Rayner, P. J., Baker, D., Bousquet, P., Bruhwiler, L., Chen, Y.-H., Ciais, P., Fan, S., Fung, I. Y., Gloor, M., Heimann, M., Higuchi, K., John, J., Maki, T., Maksyutov, S., Masarie, K., Peylin, P., Prather, M., Pak, B. C., Randerson, J., Sarmiento, J., Taguchi, S., Takahashi, T., and Yuen, C.-W.: Towards robust regional estimates of CO_2 sources and sinks using atmospheric transport models, Nature, 415, 626–630, 2002.

Gurney, K. R., Law, R. M., Denning, A. S., Rayner, P. J., Pak, B. C., Baker, D., Bousquet, P., Bruhwiler, L., Chen, Y.-H., Ciais, P., Fung, I. Y., Heimann, M., John, J., Maki, T., Maksyutov, S., Peylin, P., Prather, M., and Taguchi, S.: Transcom 3 inversion intercomparison: model mean results for the estimation of seasonal carbon sources and sinks, Global Biogeochem. Cy., 18, GB1010, doi:10.1029/2003gb002111, 2004.

Hall, T. M. and Plumb, R. A.: Age as a diagnostic of stratospheric transport, J. Geophys. Res.-Atmos., 99, 1059–1070, doi:10.1029/93jd03192, 1994.

Heald, C. L., Jacob, D. J., Park, R. J., Russell, L. M., Huebert, B. J., Seinfeld, J. H., Liao, H., and Weber, R. J.: A large organic aerosol source in the free troposphere missing from current models, Geophys. Res. Lett., 32, L18809, doi:10.1029/2005gl023831, 2005.

Henze, D. K., Hakami, A., and Seinfeld, J. H.: Development of the adjoint of GEOS-Chem, Atmos. Chem. Phys., 7, 2413–2433, doi:10.5194/acp-7-2413-2007, 2007.

Henze, D. K., Seinfeld, J. H., and Shindell, D. T.: Inverse modeling and mapping US air quality influences of inorganic $PM_{2.5}$ precursor emissions using the adjoint of GEOS-Chem, Atmos. Chem. Phys., 9, 5877–5903, doi:10.5194/acp-9-5877-2009, 2009.

Holzer, M. and Hall, T. M.: Tropospheric transport climate partitioned by surface origin and transit time, J. Geophys. Res.-Atmos., 113, D08104, doi:10.1029/2007jd009115, 2008.

Houweling, S., Breon, F.-M., Aben, I., Rödenbeck, C., Gloor, M., Heimann, M., and Ciais, P.: Inverse modeling of CO_2 sources and sinks using satellite data: a synthetic inter-comparison of measurement techniques and their performance as a function of space and time, Atmos. Chem. Phys., 4, 523–538, doi:10.5194/acp-4-523-2004, 2004.

Title Page

Abstract | Introduction

Conclusions | References

Tables | Figures

◄ | ►

◄ | ►

Back | Close

Full Screen / Esc

Printer-friendly Version

Interactive Discussion

Jiang, Z., Jones, D. B. A., Kopacz, M., Liu, J., Henze, D. K., and Heald, C.: Quantifying the impact of model errors on top-down estimates of carbon monoxide emissions using satellite observations, J. Geophys. Res., 116, D15306, doi:10.1029/2010jd015282, 2011.

Jones, C., McConnell, C., Coleman, K., Cox, P., Falloon, P., Jenkinson, D., and Powlson, D.: Global climate change and soil carbon stocks; predictions from two contrasting models for the turnover of organic carbon in soil, Glob. Change Biol., 11, 154–166, 2005.

Jung, M., Reichstein, M., and Bondeau, A.: Towards global empirical upscaling of FLUXNET eddy covariance observations: validation of a model tree ensemble approach using a biosphere model, Biogeosciences, 6, 2001–2013, doi:10.5194/bg-6-2001-2009, 2009.

Jung, M., Reichstein, M., Margolis, H. A., Cescatti, A., Richardson, A. D., Arain, M. A., Arneth, A., Bernhofer, C., Bonal, D., Chen, J., Gianelle, D., Gobron, N., Kiely, G., Kutsch, W., Lasslop, G., Law, B. E., Lindroth, A., Merbold, L., Montagnani, L., Moors, E. J., Papale, D., Sottocornola, M., Vaccari, F., and Williams, C.: Global patterns of land-atmosphere fluxes of carbon dioxide, latent heat, and sensible heat derived from eddy covariance, satellite, and meteorological observations, J. Geophys. Res.-Biogeo., 116, G00J07, doi:10.1029/2010jg001566, 2011.

Kalnay, E., Kanamitsu, M., Kistler, R., Collins, W., Deaven, D., Gandin, L., Iredell, M., Saha, S., White, G., Woollen, J., Zhu, Y., Leetmaa, A., Reynolds, R., Chelliah, M., Ebisuzaki, W., Higgins, W., Janowiak, J., Mo, K. C., Ropelewski, C., Wang, J., Jenne, R., and Joseph, D.: The NCEP/NCAR 40-year reanalysis project, B. Am. Meteorol. Soc., 77, 437–471, doi:10.1175/1520-0477(1996)077<0437:TNYRP>2.0.CO;2, 1996.

Kim, B. Y., Fleming, G. G., Lee, J. J., Waitz, I. A., Clarke, J.-P., Balasubramanian, S., Malwitz, A., Klima, K., Locke, M., Holsclaw, C. A., Maurice, L. Q., and Gupta, M. L.: System for assessing Aviation's Global Emissions (SAGE), Part 1: Model description and inventory results, Transport. Res. D-Tr. E., 12, 325–346, doi:10.1016/j.trd.2007.03.007, 2007.

Kopacz, M., Jacob, D. J., Henze, D. K., Heald, C. L., Streets, D. G., and Zhang, Q.: Comparison of adjoint and analytical Bayesian inversion methods for constraining Asian sources of carbon monoxide using satellite (MOPITT) measurements of CO columns, J. Geophys. Res., 114, D04305, doi:10.1029/2007jd009264, 2009.

Kopacz, M., Mauzerall, D. L., Wang, J., Leibensperger, E. M., Henze, D. K., and Singh, K.: Origin and radiative forcing of black carbon transported to the Himalayas and Tibetan Plateau, Atmos. Chem. Phys., 11, 2837–2852, doi:10.5194/acp-11-2837-2011, 2011.

Title Page

Abstract | Introduction

Conclusions | References

Tables | Figures

◄◄ | ►►

◄ | ►

Back | Close

Full Screen / Esc

Printer-friendly Version

Interactive Discussion

Kuze, A., Suto, H., Nakajima, M., and Hamazaki, T.: Thermal and near infrared sensor for carbon observation Fourier-transform spectrometer on the Greenhouse Gases Observing Satellite for greenhouse gases monitoring, Appl. Optics, 48, 6716–6733, 2009.

Law, R. M., Chen, Y.-H., Gurney, K. R., and Modellers, T.: TransCom 3 CO_2 inversion inter-comparison: 2. sensitivity of annual mean results to data choices, Tellus B, 55, 580–595, 2003.

Li, Q., Jacob, D. J., Bey, I., Palmer, P. I., Duncan, B. N., Field, B. D., Martin, R. V., Fiore, A. M., Yantosca, R. M., Parrish, D. D., Simmonds, P. G., and Oltmans, S. J.: Transatlantic transport of pollution and its effects on surface ozone in Europe and North America, J. Geophys. Res.-Atmos., 107, ACH 4-1–ACH 4-21, doi:10.1029/2001jd001422, 2002.

Liu, D. C. and Nocedal, J.: On the limited memory BFGS method for large scale optimization, Math. Program., 45, 503–528, doi:10.1007/bf01589116, 1989.

Maksyutov, S., Takagi, H., Valsala, V. K., Saito, M., Oda, T., Saeki, T., Belikov, D. A., Saito, R., Ito, A., Yoshida, Y., Morino, I., Uchino, O., Andres, R. J., and Yokota, T.: Regional CO_2 flux estimates for 2009–2010 based on GOSAT and ground-based CO_2 observations, Atmos. Chem. Phys., 13, 9351–9373, doi:10.5194/acp-13-9351-2013, 2013.

Marland, G.: Uncertainties in accounting for CO_2 from fossil fuels, J. Ind. Ecol., 12, 136–139, 2008.

Messerschmidt, J., Geibel, M. C., Blumenstock, T., Chen, H., Deutscher, N. M., Engel, A., Feist, D. G., Gerbig, C., Gisi, M., Hase, F., Katrynski, K., Kolle, O., Lavrič, J. V., Notholt, J., Palm, M., Ramonet, M., Rettinger, M., Schmidt, M., Sussmann, R., Toon, G. C., Truong, F., Warneke, T., Wennberg, P. O., Wunch, D., and Xueref-Remy, I.: Calibration of TCCON column-averaged CO_2: the first aircraft campaign over European TCCON sites, Atmos. Chem. Phys., 11, 10765–10777, doi:10.5194/acp-11-10765-2011, 2011.

Michalak, A. M., Hirsch, A., Bruhwiler, L., Gurney, K. R., Peters, W., and Tans, P. P.: Maximum likelihood estimation of covariance parameters for Bayesian atmospheric trace gas surface flux inversions, J. Geophys. Res., 110, D24107, doi:10.1029/2005jd005970, 2005.

Müller, J.-F. and Stavrakou, T.: Inversion of CO and NO_x emissions using the adjoint of the IMAGES model, Atmos. Chem. Phys., 5, 1157–1186, doi:10.5194/acp-5-1157-2005, 2005.

Nassar, R., Jones, D. B. A., Suntharalingam, P., Chen, J. M., Andres, R. J., Wecht, K. J., Yantosca, R. M., Kulawik, S. S., Bowman, K. W., Worden, J. R., Machida, T., and Mat-sueda, H.: Modeling global atmospheric CO_2 with improved emission inventories and CO_2

production from the oxidation of other carbon species, Geosci. Model Dev., 3, 689–716, doi:10.5194/gmd-3-689-2010, 2010.

Nassar, R., Jones, D. B. A., Kulawik, S. S., Worden, J. R., Bowman, K. W., Andres, R. J., Suntharalingam, P., Chen, J. M., Brenninkmeijer, C. A. M., Schuck, T. J., Conway, T. J., and Worthy, D. E.: Inverse modeling of CO_2 sources and sinks using satellite observations of CO_2 from TES and surface flask measurements, Atmos. Chem. Phys., 11, 6029–6047, doi:10.5194/acp-11-6029-2011, 2011.

O'Dell, C. W., Connor, B., Bösch, H., O'Brien, D., Frankenberg, C., Castano, R., Christi, M., Eldering, D., Fisher, B., Gunson, M., McDuffie, J., Miller, C. E., Natraj, V., Oyafuso, F., Polonsky, I., Smyth, M., Taylor, T., Toon, G. C., Wennberg, P. O., and Wunch, D.: The ACOS CO_2 retrieval algorithm – Part 1: Description and validation against synthetic observations, Atmos. Meas. Tech., 5, 99–121, doi:10.5194/amt-5-99-2012, 2012.

Palmer, P. I., Jacob, D. J., Fiore, A. M., Martin, R. V., Chance, K., and Kurosu, T. P.: Mapping isoprene emissions over North America using formaldehyde column observations from space, J. Geophys. Res.-Atmos., 108, 4180–4192, doi:10.1029/2002jd002153, 2003.

Park, B. C. and Prather, M. J.: CO_2 source inversions using satellite observations of the upper troposphere, Geophys. Res. Lett., 28, 4571–4574, doi:10.1029/2001gl013604, 2001.

Patra, P. K., Maksyutov, S., Ishizawa, M., Nakazawa, T., Takahashi, T., and Ukita, J.: Interannual and decadal changes in the sea-air CO_2 flux from atmospheric CO_2 inverse modeling, Global Biogeochem. Cy., 19, GB4013, doi:10.1029/2004gb002257, 2005.

Peters, W., Jacobson, A. R., Sweeney, C., Andrews, A. E., Conway, T. J., Masarie, K., Miller, J. B., Bruhwiler, L. M. P., Pétron, G., Hirsch, A. I., Worthy, D. E. J., van der Werf, G. R., Randerson, J. T., Wennberg, P. O., Krol, M. C., and Tans, P. P.: An atmospheric perspective on North American carbon dioxide exchange: CarbonTracker, P. Natl. Acad. Sci. USA, 104, 18925–18930, doi:10.1073/pnas.0708986104, 2007.

Peters, W., Krol, M. C., Van Der Werf, G. R., Houweling, S., Jones, C. D., Hughes, J., Schaefer, K., Masarie, K. A., Jacobson, A. R., Miller, J. B., Cho, C. H., Ramonet, M., Schmidt, M., Ciattaglia, L., Apadula, F., Heltai, D., Meinhardt, F., Di Sarra, A. G., Piacentino, S., Sferlazzo, D., Aalto, T., Hatakka, J., Ström, J., Haszpra, L., Meijer, H. A. J., Van Der Laan, S., Neubert, R. E. M., Jordan, A., Rodó, X., Morguí, J. A., Vermeulen, A. T., Popa, E., Rozanski, K., Zimnoch, M., Manning, A. C., Leuenberger, M., Uglietti, C., Dolman, A. J., Ciais, P., Heimann, M., and Tans, P. P.: Seven years of recent European net terrestrial carbon diox-

ide exchange constrained by atmospheric observations, Glob. Change Biol., 16, 1317–1337, doi:10.1111/j.1365-2486.2009.02078.x, 2010.

Peylin, P., Baker, D., Sarmiento, J., Ciais, P., and Bousquet, P.: Influence of transport uncertainty on annual mean and seasonal inversions of atmospheric CO_2 data, J. Geophys. Res., 107, 4385–4409, doi:10.1029/2001jd000857, 2002.

Randerson, J. T., Hoffman, F. M., Thornton, P. E., Mahowald, N. M., Lindsay, K., Lee, Y.-H., Nevison, C. D., Doney, S. C., Bonan, G., Stöckli, R., Covey, C., Running, S. W., and Fung, I. Y.: Systematic assessment of terrestrial biogeochemistry in coupled climate-carbon models, Glob. Change Biol., 15, 2462–2484, doi:10.1111/j.1365-2486.2009.01912.x, 2009.

Rayner, P. J., Enting, I. G., Francey, R. J., and Langenfelds, R.: Reconstructing the recent carbon cycle from atmospheric CO_2, $\delta^{13}C$ and O_2/N_2 observations, Tellus B, 51, 213–232, doi:10.1034/j.1600-0889.1999.t01-1-00008.x, 1999.

Rayner, P. J. and O'Brien, D. M.: The utility of remotely sensed CO_2 concentration data in surface source inversions, Geophys. Res. Lett., 28, 175–178, doi:10.1029/2000gl011912, 2001.

Rayner, P. J., Law, R. M., Allison, C. E., Francey, R. J., Trudinger, C. M., and Pickett-Heaps, C.: Interannual variability of the global carbon cycle (1992–2005) inferred by inversion of atmospheric CO_2 and $\delta_{13}CO_2$ measurements, Global Biogeochem. Cy., 22, GB3008, doi:10.1029/2007GB003068, 2008.

Rödenbeck, C., Houweling, S., Gloor, M., and Heimann, M.: CO_2 flux history 1982–2001 inferred from atmospheric data using a global inversion of atmospheric transport, Atmos. Chem. Phys., 3, 1919–1964, doi:10.5194/acp-3-1919-2003, 2003.

Stephens, B. B., Gurney, K. R., Tans, P. P., Sweeney, C., Peters, W., Bruhwiler, L., Ciais, P., Ramonet, M., Bousquet, P., Nakazawa, T., Aoki, S., Machida, T., Inoue, G., Vinnichenko, N., Lloyd, J., Jordan, A., Heimann, M., Shibistova, O., Langenfelds, R. L., Steele, L. P., Francey, R. J., and Denning, A. S.: Weak northern and strong tropical land carbon uptake from vertical profiles of atmospheric CO_2, Science, 316, 1732–1735, doi:10.1126/science.1137004, 2007.

Takagi, H., Saeki, T., Oda, T., Saito, M., Valsala, V., Belikov, D., Saito, R., Yoshida, Y., Morino, I., Uchino, O., Andres, R. J., Yokota, T., and Maksyutov, S.: On the benefit of GOSAT observations to the estimation of regional CO_2 fluxes, Sola, 7, 161–164, doi:10.2151/sola.2011-041, 2011.

Title Page

Abstract | Introduction

Conclusions | References

Tables | Figures

|◄ | ►|

◄ | ►

Back | Close

Full Screen / Esc

Printer-friendly Version

Interactive Discussion

Takahashi, T., Sutherland, S. C., Wanninkhof, R., Sweeney, C., Feely, R. A., Chipman, D. W., Hales, B., Friederich, G., Chavez, F., Sabine, C., Watson, A., Bakker, D. C. E., Schuster, U., Metzl, N., Yoshikawa-Inoue, H., Ishii, M., Midorikawa, T., Nojiri, Y., Körtzinger, A., Steinhoff, T., Hoppema, M., Olafsson, J., Arnarson, T. S., Tilbrook, B., Johannessen, T., Olsen, A., Bellerby, R., Wong, C. S., Delille, B., Bates, N. R., and de Baar, H. J. W.: Climatological mean and decadal change in surface ocean pCO_2, and net sea-air CO_2 flux over the global oceans, Deep-Sea Res. Pt. II, 56, 554–577, 2009.

Tarantola, A.: Inverse Problem Theory and Methods for Model Parameter Estimation, Society for Industrial and Applied Mathematics, Philadelphia, PA, USA, 2004.

Thompson, J. E., Hayes, P. L., Jimenez, J. L., Adachi, K., Zhang, X., Liu, J., Weber, R. J., and Buseck, P. R.: Aerosol optical properties at Pasadena, CA during CalNex 2010, Atmos. Environ., 55, 190–200, doi:10.1016/j.atmosenv.2012.03.011, 2012.

van der Werf, G. R., Randerson, J. T., Giglio, L., Collatz, G. J., Mu, M., Kasibhatla, P. S., Morton, D. C., DeFries, R. S., Jin, Y., and van Leeuwen, T. T.: Global fire emissions and the contribution of deforestation, savanna, forest, agricultural, and peat fires (1997–2009), Atmos. Chem. Phys., 10, 11707–11735, doi:10.5194/acp-10-11707-2010, 2010.

Washenfelder, R. A., Toon, G. C., Blavier, J. F., Yang, Z., Allen, N. T., Wennberg, P. O., Vay, S. A., Matross, D. M., and Daube, B. C.: Carbon dioxide column abundances at the Wisconsin Tall Tower site, J. Geophys. Res., 111, D22305, doi:10.1029/2006jd007154, 2006.

Wilkerson, J. T., Jacobson, M. Z., Malwitz, A., Balasubramanian, S., Wayson, R., Fleming, G., Naiman, A. D., and Lele, S. K.: Analysis of emission data from global commercial aviation: 2004 and 2006, Atmos. Chem. Phys., 10, 6391–6408, doi:10.5194/acp-10-6391-2010, 2010.

Wofsy, S. C., Team, H. S., Cooperating, M., and Satellite, T.: HIAPER Pole-to-Pole Observations (HIPPO): fine-grained, global-scale measurements of climatically important atmospheric gases and aerosols, Philos. T. R. Soc. A, 369, 2073–2086, doi:10.1098/rsta.2010.0313, 2011.

Wunch, D., Toon, G. C., Wennberg, P. O., Wofsy, S. C., Stephens, B. B., Fischer, M. L., Uchino, O., Abshire, J. B., Bernath, P., Biraud, S. C., Blavier, J.-F. L., Boone, C., Bowman, K. P., Browell, E. V., Campos, T., Connor, B. J., Daube, B. C., Deutscher, N. M., Diao, M., Elkins, J. W., Gerbig, C., Gottlieb, E., Griffith, D. W. T., Hurst, D. F., Jiménez, R., Keppel-Aleks, G., Kort, E. A., Macatangay, R., Machida, T., Matsueda, H., Moore, F., Morino, I., Park, S., Robinson, J., Roehl, C. M., Sawa, Y., Sherlock, V., Sweeney, C., Tanaka, T., and

Title Page

Abstract | Introduction

Conclusions | References

Tables | Figures

|◀ | ▶|

◀ | ▶

Back | Close

Full Screen / Esc

Printer-friendly Version

Interactive Discussion

Zondlo, M. A.: Calibration of the Total Carbon Column Observing Network using aircraft profile data, Atmos. Meas. Tech., 3, 1351–1362, doi:10.5194/amt-3-1351-2010, 2010.

Wunch, D., Wennberg, P. O., Toon, G. C., Connor, B. J., Fisher, B., Osterman, G. B., Frankenberg, C., Mandrake, L., O'Dell, C., Ahonen, P., Biraud, S. C., Castano, R., Cressie, N., Crisp, D., Deutscher, N. M., Eldering, A., Fisher, M. L., Griffith, D. W. T., Gunson, M., Heikkinen, P., Keppel-Aleks, G., Kyrö, E., Lindenmaier, R., Macatangay, R., Mendonca, J., Messerschmidt, J., Miller, C. E., Morino, I., Notholt, J., Oyafuso, F. A., Rettinger, M., Robinson, J., Roehl, C. M., Salawitch, R. J., Sherlock, V., Strong, K., Sussmann, R., Tanaka, T., Thompson, D. R., Uchino, O., Warneke, T., and Wofsy, S. C.: A method for evaluating bias in global measurements of CO_2 total columns from space, Atmos. Chem. Phys., 11, 12317–12337, doi:10.5194/acp-11-12317-2011, 2011.

Yevich, R. and Logan, J. A.: An assessment of biofuel use and burning of agricultural waste in the developing world, Global Biogeochem. Cy., 17, 1095–1134, doi:10.1029/2002gb001952, 2003.

Zhao, C. L. and Tans, P. P.: Estimating uncertainty of the WMO mole fraction scale for carbon dioxide in air, J. Geophys. Res., 111, D08S09, doi:10.1029/2005jd006003, 2006.

Table 1. Summary of emission inventories of 2010 used in our GEOS-Chem CO_2 model simulation.

Flux type	Inventory data description	2010 global annual flux (Pg C)
Fuel and cement manufacture	Carbon Dioxide Information Analysis Center (CDIAC) 1˚ × 1˚ monthly fossil fuel and cement manufacture CO_2 emissions	8.54
Shipping	monthly shipping emission of CO_2 from International Comprehensive Ocean–Atmosphere Data Set (ICOADS)	0.19
Aviation	3-D aviation CO_2 emissions based on 2˚ × 2.5˚ gridded flight track density	0.16
Biomass burning	monthly biomass burning CO_2 emissions available from the Global Emissions Fire Database version 3 (GFEDv3)	1.84
Biofuel burning	biofuel (heating/cooking) CO_2 emission estimated by Yevich and Logan	0.86
Balanced biosphere	the 3 hourly terrestrial ecosystem exchange produced by BEPS	0.00
Ocean exchange	the climatology of monthly ocean-atmosphere CO_2 flux by Takahashi et al.	−1.41

Table 2. The mean, standard deviation (STDV), and the mean absolute value (MAV) of the a posteriori model – observation mismatch in 2010 for the four flask sites listed in Fig. 8, and for the global average of the 78 flask sites shown in Fig. 2.

Site Code	RUN_A			RUN_B			RUN_C		
	mean	STDV	MAV	mean	STDV	MAV	mean	STDV	MAV
ALT	−0.52	1.08	0.91	−0.17	1.23	0.87	−0.42	1.14	0.83
MLO[a]	−0.14	0.92	0.72	−0.16	1.12	0.85	−0.11	0.99	0.75
GMI	−0.04	0.89	0.70	−0.07	0.88	0.69	0.11	0.91	0.70
CGO	−1.18	0.51	1.18	−1.19	0.41	1.19	−0.68	0.35	0.69
78 sites	0.07	5.32	2.67	0.05	5.47	2.74	0.01	5.36	2.62

[a] MLO observatory is at an altitude of 3397 m and it is probably not resolved well in our posterior simulations (Nassar et al., 2010).

Table 3. The mean difference, standard deviation (STDV), and the mean absolute value (MAV) of the model – observation mismatch for 13 TCCON sites in 2010. Also listed are the averages and correlation for all 13 sites.

Site	RUN_A			RUN_B			RUN_C		
	mean	STDV	MAV	mean	STDV	MAV	mean	STDV	MAV
Lamont	−0.48	1.03	0.89	−1.05	1.15	1.24	−0.72	0.95	0.92
Park Falls	−0.29	0.96	0.81	−0.31	0.92	0.77	−0.29	0.82	0.69
Eureka	1.10	1.05	1.25	0.93	0.89	1.04	0.94	0.95	1.08
Izana[a]	−0.46	0.49	0.55	−1.12	0.61	1.15	−0.68	0.51	0.74
Orleans	−0.41	0.88	0.79	−0.55	0.77	0.78	−0.26	0.84	0.70
Karlsruhe	0.62	1.25	1.04	−0.28	1.05	0.82	0.16	1.00	0.73
Bremen	−0.82	1.02	1.08	−1.16	1.34	1.40	−0.97	1.29	1.27
Garmisch	1.16	1.47	1.47	0.48	1.02	0.88	0.67	1.02	0.96
Bialystok	0.66	1.27	1.08	0.20	1.39	1.03	0.60	1.18	1.02
Sodankylä	1.11	0.86	1.22	0.99	0.92	1.17	1.15	0.85	1.27
Darwin	0.11	0.52	0.41	0.07	0.50	0.39	0.65	0.43	0.69
Wollongong	0.81	0.65	0.91	0.61	0.68	0.79	1.09	0.65	1.15
Lauder	0.18	0.76	0.60	0.03	0.74	0.57	0.48	0.74	0.70
All 13 sites	0.16	1.22	0.95	−0.23	1.24	0.98	0.06	1.15	0.91
r^2		0.77			0.76			0.80	

[a] Izana is at an altitude of 2370 m and it is probably not resolved well in our posterior simulations.

Table 4. The mean difference, standard deviation (STDV), and the mean absolute value (MAV) of the model – observation mismatch for HIPPO-3 observations.

|	mean	STDV	MAV
RUN_A	−0.07	1.37	1.02
RUN_B	−0.08	1.39	1.05
RUN_C	−0.17	1.33	0.97
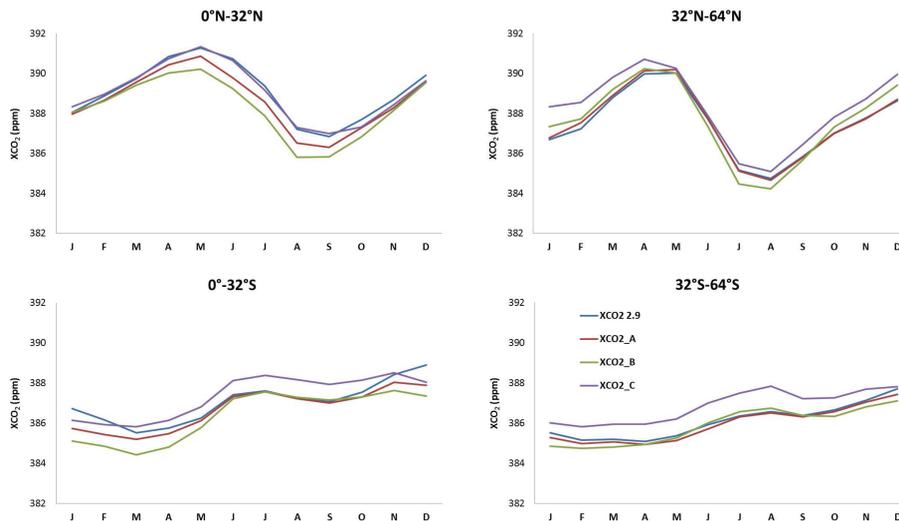
Fig. 1. Monthly mean, zonally averaged XCO_2 data from GOSAT, binned in latitude between 32°–64° N, 0°–32° N, 32° S–0°, and 64° S–32° S. Shown are the XCO_2 data (version b2.9) before additional filtering and bias correction (blue lines), and XCO2_A, XCO2_B, and XCO2_C (version b2.10) for the three different bias correction schemes employed.
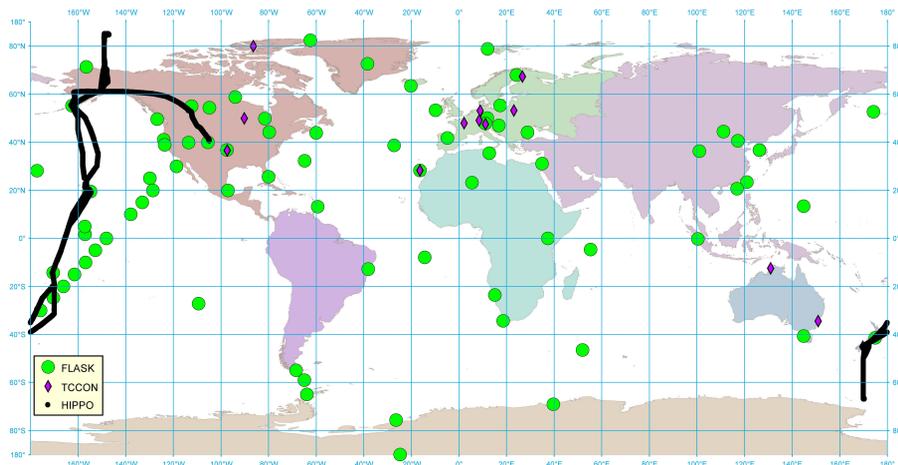
Fig. 2. Global distribution of CO_2 flask sample collection locations from 72 NOAA ESRL Carbon Cycle Cooperative Global Air Sampling Network sites and 6 Environment Canada (EC) sampling sites (green solid symbols), 13 TCCON observatories (purple diamond symbols), and aircraft sampling locations from HIPPO-3 campaign (black dot symbols).
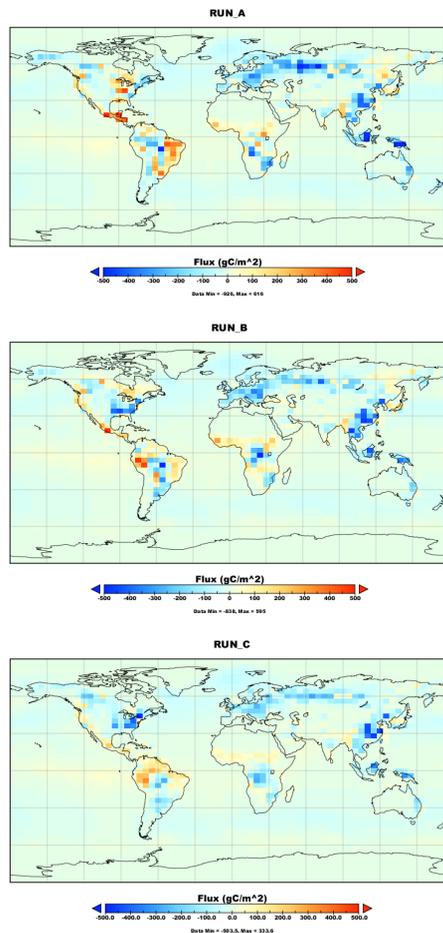
Fig. 3. Annual global surface fluxes of CO_2 in $g\,C\,m^{-2}$ for the inversion analyses RUN_A, RUN_B, and RUN_C.

Title Page

Abstract | Introduction

Conclusions | References

Tables | Figures

|◀ | ▶|

◀ | ▶

Back | Close

Full Screen / Esc

Printer-friendly Version

Interactive Discussion

Fig. 4. Annual fluxes for 11 TranCom regions inferred from three XCO$_2$ datasets. The a priori fluxes (the sum of all prior fluxes excluding emissions from the fossil fuel burning) are also indicated.
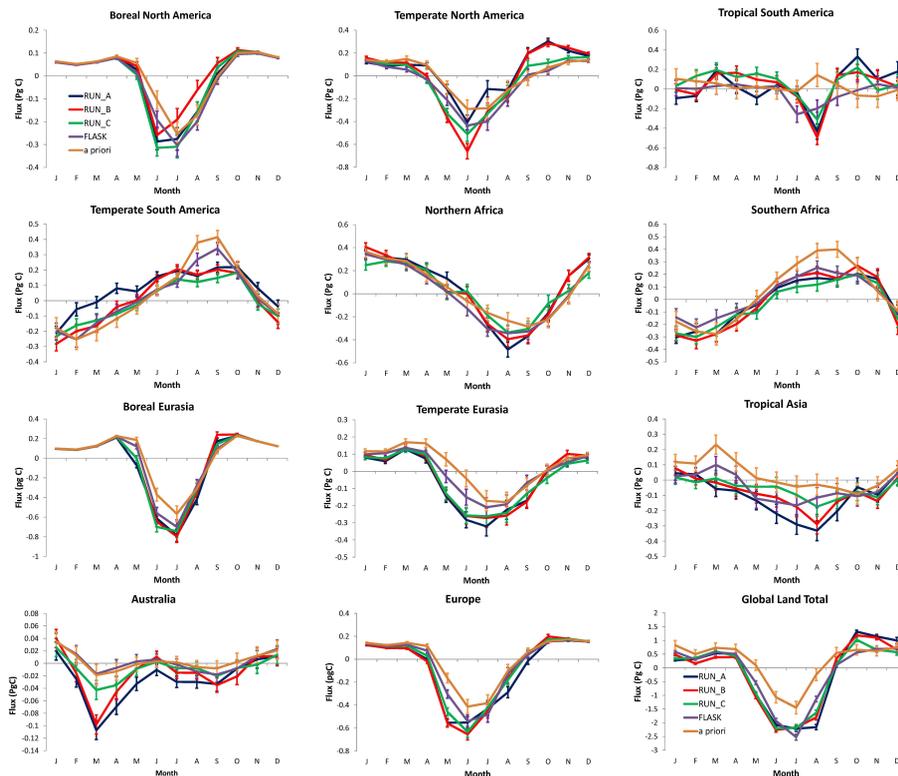
Fig. 5. Monthly fluxes and their uncertainties for 11 TranCom 3 regions and global land surface inferred from three XCO$_2$ datasets (RUN_A (blue), RUN_B (red), and RUN_C (green)), and Flask observations (FLASK, purple). The a priori fluxes (the sum of all prior fluxes excluding emissions from the fossil fuel burning) are also indicated (a priori, orange).

Title Page

Abstract | Introduction

Conclusions | References

Tables | Figures

|◄ | ►|

◄ | ►

Back | Close

Full Screen / Esc

Printer-friendly Version

Interactive Discussion
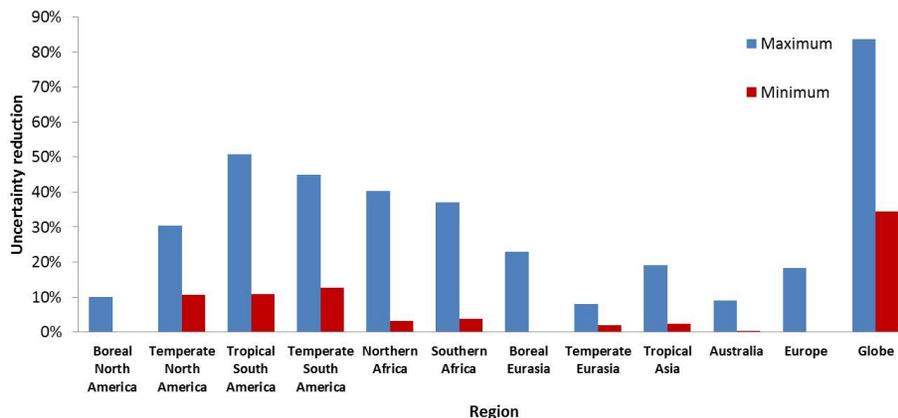
Fig. 6. The maximum and minimum uncertainty reduction on the monthly mean flux estimates aggregated to the TransCom regions. For a given region, the maximum value represents the largest uncertainty reduction obtained for any month in 2010, whereas the minimum value is the small uncertainty reduction obtained in any month in 2010.
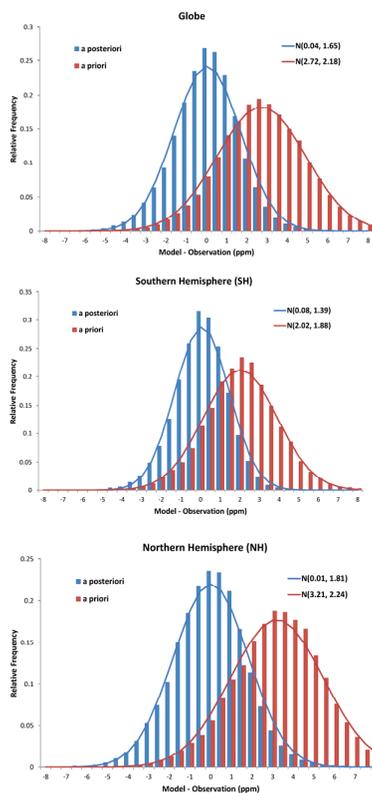
Fig. 7. The distribution of the modeled minus observed XCO_2 in ppm. The red bars are from the modeled a priori XCO_2 minus the observed XCO_2, whereas the blue bars are from the modeled a posteriori XCO_2 minus the observed XCO_2. The blue and red solid lines show a normal distribution for the a priori and a posteriori differences. The distribution means and the standard deviations are indicated.

Title Page

Abstract | Introduction

Conclusions | References

Tables | Figures

|◄ | ►|

◄ | ►

Back | Close

Full Screen / Esc

Printer-friendly Version

Interactive Discussion
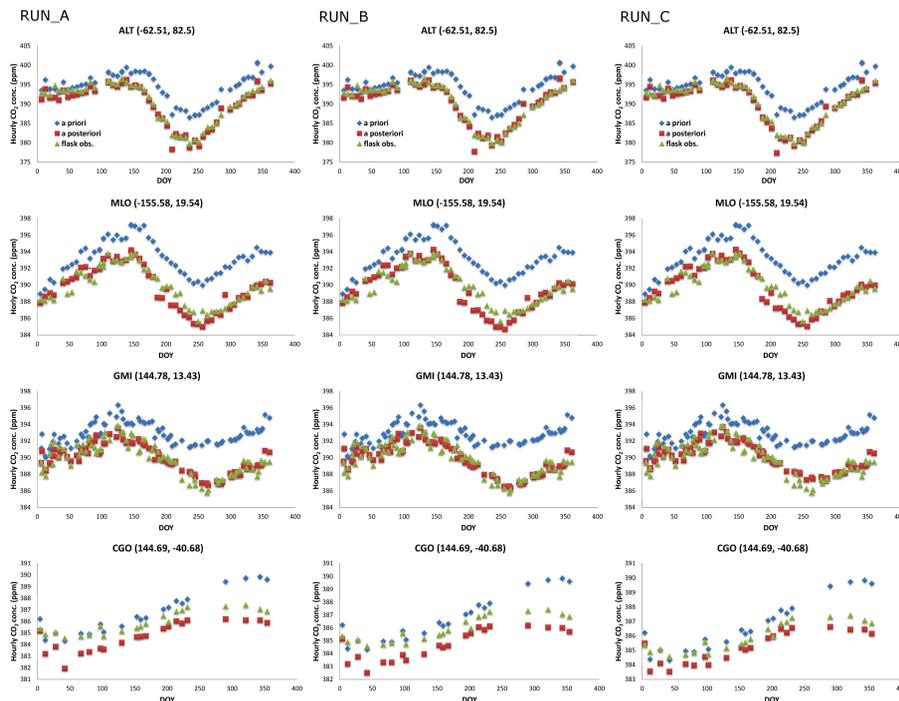
Fig. 8. The a priori (blue diamonds), and a posteriori (red squares) modeled observations, and real flask observations (green triangles) for 4 selected sites for RUN_A, RUN_B, and RUN_C. These a priori and a posteriori simulations use the original initial field that differ from those used for the inverse modeling. Site code (longitude, latitude) is shown as the title of each chart.

Title Page

Abstract | Introduction

Conclusions | References

Tables | Figures

|◀ | ▶|

◀ | ▶

Back | Close

Full Screen / Esc

Printer-friendly Version

Interactive Discussion
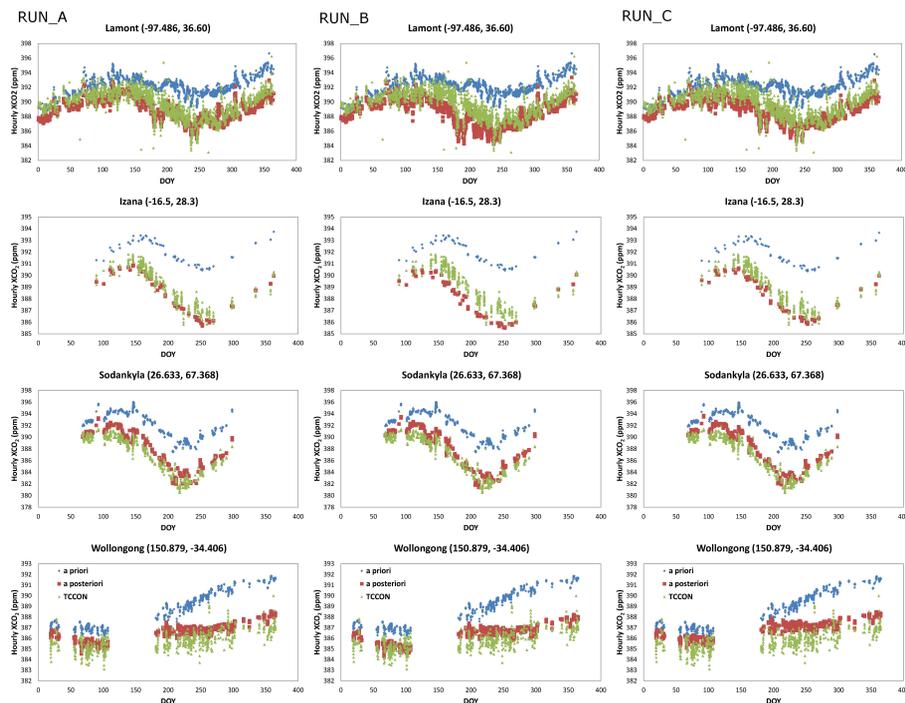
Fig. 9. The TCCON XCO$_2$ (green) for four selected sites and the a priori (blue) and a posteriori (red) XCO$_2$ for for RUN_A, RUN_B, and RUN_C. The a priori and a posteriori simulations used the original initial CO$_2$ field that was not scaled to remove the global offset relative to the GOSAT XCO$_2$.

Discussion Paper | Discussion Paper | Discussion Paper | Discussion Paper |

ACPD

13, 26327–26388, 2013

Inferring CO$_2$ fluxes from GOSAT XCO$_2$

F. Deng et al.

Title Page

Abstract   Introduction

Conclusions   References

Tables   Figures

|◀   ▶|

◀   ▶

Back   Close

Full Screen / Esc

Printer-friendly Version

Interactive Discussion
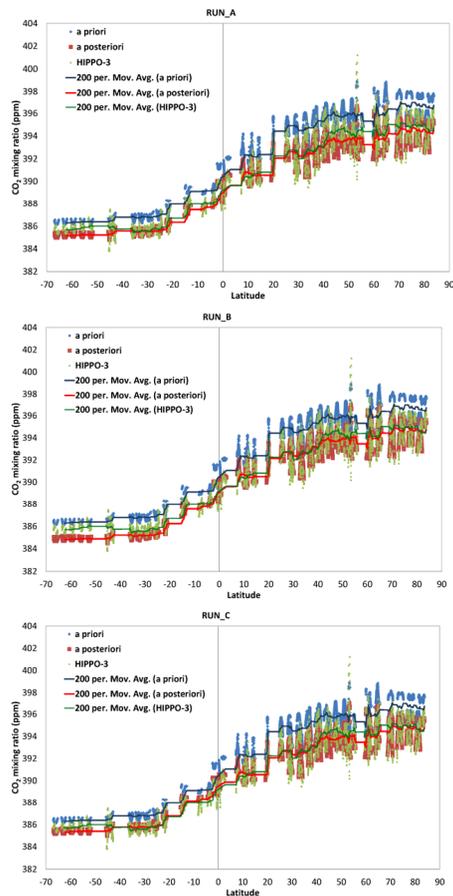
Fig. 10. Comparison of modeled a priori (blue) and a posteriori (red) CO_2 mixing ratios with HIPPO observations (green) between 70° S to 84° N and 1000 m to 5000 m. The a priori and a posteriori simulations use the original initial CO_2 field that was not adjusted to remove the global bias relative to the GOSAT XCO$_2$ data.

Title Page

Abstract | Introduction

Conclusions | References

Tables | Figures

◀ | ▶

◄ | ►

Back | Close

Full Screen / Esc

Printer-friendly Version

Interactive Discussion
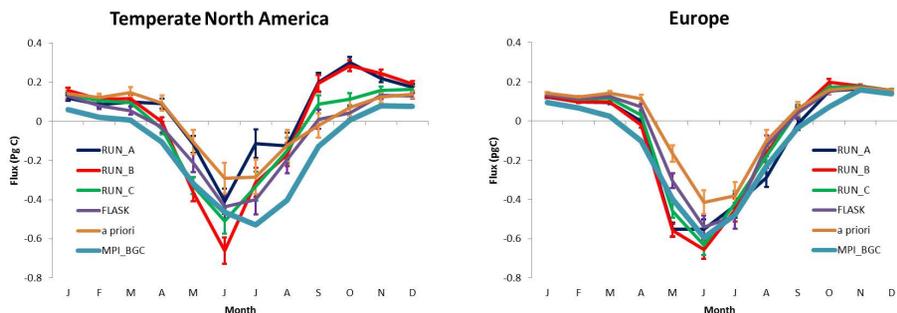
Fig. 11. Monthly fluxes and their uncertainties, as in Fig. 5, for Temperate North America and Europe. Shown are the fluxes inferred from the three XCO$_2$ datasets (RUN_A, RUN_B, and RUN_C), and the flask observations (FLASK). Also plotted are the flux estimates from the MPI-BGC flux data product. The a priori fluxes (the sum of all prior fluxes excluding emissions from the fossil fuel burning) are also indicated (a priori).
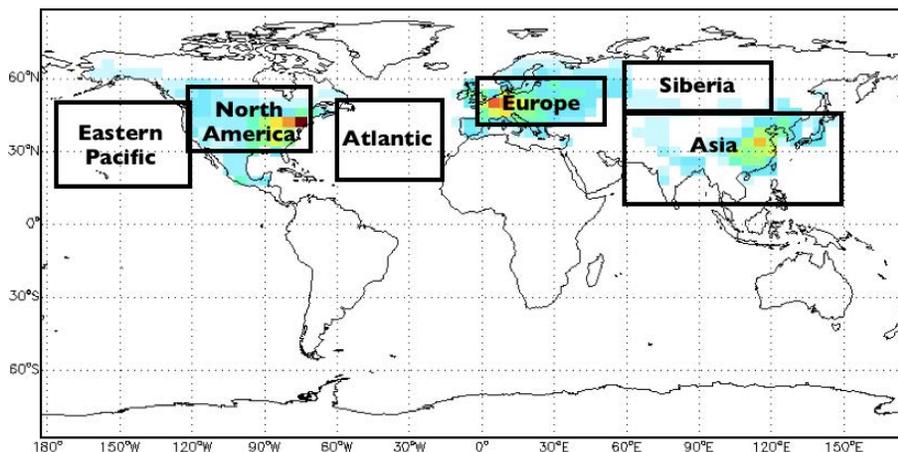
Fig. 12. Distribution of CO$_2$ fluxes in North America, Europe, and Asia used for the pulse experiment to simulate the sensitivities of the modeled XCO$_2$ to the regional fluxes, using Eq. (17). The flux pattern represents the combined influence of the fluxes from the biosphere, fossil fuel combustion, biomass burning, and biofuel combustion, all scaled to a total flux of 1 PgC for each continental region. The black boxes represent the receptor regions used for the transit time analysis shown in Fig. 15.

Full Screen / Esc
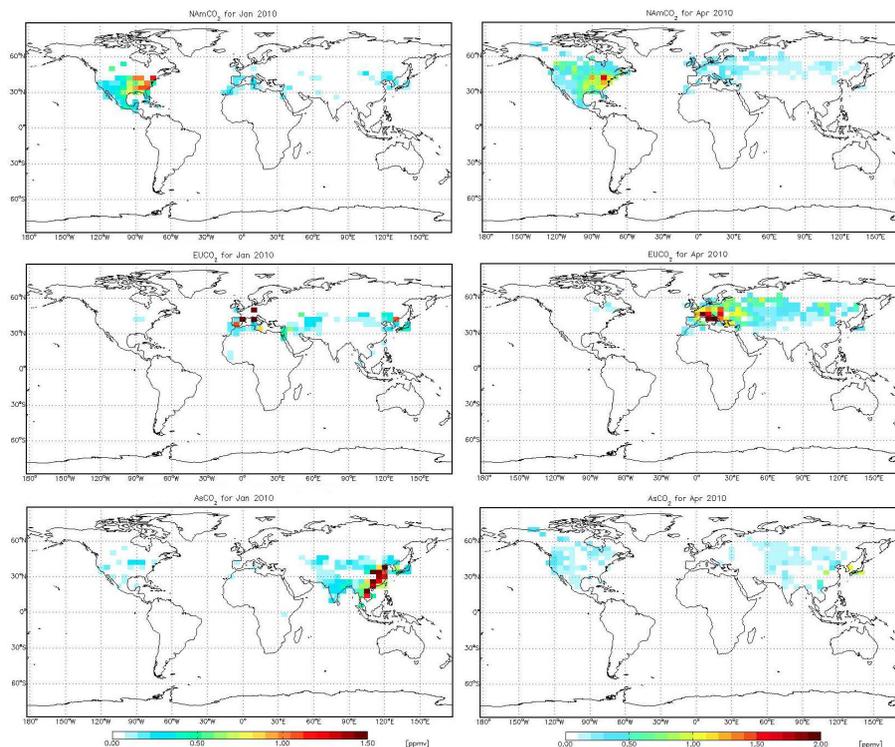
Fig. 13. Sensitivity of modeled XCO$_2$ to CO$_2$ fluxes (ppm Pg^{-1} C per month) for North America (top row), Europe (middle row), and Asia (bottom row). Shown are the sensitivities of XCO$_2$ in January (left column) and April (right column) to fluxes in January and April, respectively.
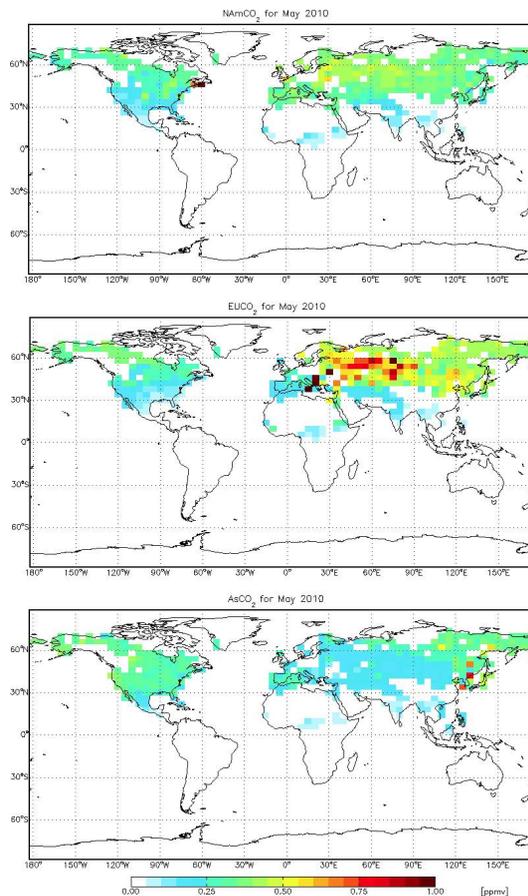
Fig. 14. Sensitivity of modeled XCO$_2$ to CO$_2$ fluxes (ppm Pg^{-1} C per month) for North America (top row), Europe (middle row), and Asia (bottom row). Shown are the sensitivities of XCO$_2$ in May to fluxes in April.
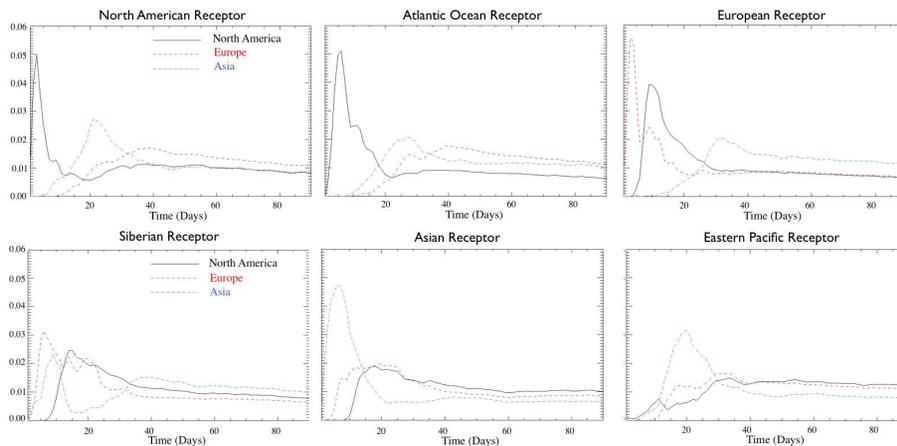
Fig. 15. Transit times (in days) of North American, European, and Asian CO_2 to the middle troposphere of the receptor regions shown in Fig. 12. The transit times were estimated using a pulse release of CO_2 of 1 PgC over one day from each continental region. The resulting tracer distributions were normalized such that the integral of the tracer abundance, averaged over the receptor region, for the 90 day period of the simulation is unity.

Title Page

Abstract | Introduction

Conclusions | References

Tables | Figures

|◀ | ▶|

◀ | ▶

Back | Close

Full Screen / Esc

Printer-friendly Version

Interactive Discussion